
76-81 GHz Planar Antenna Development and Utilization for Automotive Radar Applications

Master's thesis in Wireless and Photonics Engineering

DAPENG WU

76-81 GHz Planar Antenna Development and Utilization for Automotive Radar
Applications
DAPENG WU

© DAPENG WU, 2016

Department of Microtechnology and Nanoscience
Chalmers University of Technology
SE-412 96 Göteborg
Sweden
Telephone + 46 (0)31-772 1000

Abstract

Automotive radars are becoming more compact and affordable thanks to the rapid development of semiconductor technology. Nowadays most vehicles are equipped with radars to enhance safety and improve driving experiences. As an essential part of any radar sensor, antenna will largely influence the size and cost of the whole system. Therefore, the development of automotive radar antenna is a critically important topic of practical interest.

This thesis presents a 76.5 GHz microstrip comb-line antenna array utilized for a commercial automotive radar prototype. First a 13-element 90 degree comb-line array is realized in standing wave configuration so no additional reflection-cancelling structures are required. In order to achieve a trade-off between beamwidth and sidelobe level, a 20 dB Taylor amplitude taper is applied. Based on the conventional 90 degree array, a new array with 45 degree polarization is built to minimize the interference from cars moving in the opposite direction. All simulations are performed in Momentum Simulator of Advanced Design System.

The dimensions of 90 and 45 degree comb-line arrays are $20.7 \times 2.5 \text{ mm}^2$ and $20.5 \times 2.0 \text{ mm}^2$, respectively. Both of them are implemented on Rogers RO3003 substrate. A probe-based setup is employed for the measurement of S-parameter and radiation patterns. From 76 to 78 GHz, both arrays exhibit consistent performance. At 76.5 GHz, the 45 degree array yields a maximum gain of 11.35 dBi at $\theta = -1^\circ$ and a sidelobe level of -16.3 dB; the cross-polarization level is fluctuating around -10 dB. Overall, the measurement results show good agreement with simulations.

Keywords: antenna, automotive radar, microstrip, comb-line, millimeter wave

Acknowledgment

It would not have been possible to complete this thesis without the generous contributions of many great people.

First and foremost, I would like to express my sincerest gratitude to my supervisor Dr. Ralf Reuter for his immense expertise, contagious enthusiasm and tremendous patience. The valuable experiences I gained under his guidance will pave the way for my future career. I am also deeply grateful to my examiner Professor Jian Yang for providing insightful advices to improve my work and refine my thesis.

Furthermore, I am indebted to Dr. Ziqiang Tong for the helpful discussion and warm hospitality during my stay in Germany. Special thanks go out to Dr. Heiko Gulan and Dr. Christian Rusch for devoting enormous efforts to the antenna measurement.

Finally, I want to thank my family for the unconditional love and wholehearted support throughout my study.

Table of Contents

Abstract	I
Acknowledgment	II
List of Abbreviations	IV
1 Introduction	1
1.1 Overview of Automotive Radar System	1
1.2 Antennas for Automotive Radars	3
1.3 Aim of the Thesis Project.....	4
2 Analysis of Microstrip Comb-Line Antenna Array	7
2.1 Characteristics of Microstrip Open-Circuit Stub	7
2.1.1 Radiation Pattern of a Microstrip Open-Circuit Stub	7
2.1.2 Impact of Substrate Surface Waves	9
2.1.3 Improved Analysis of Microstrip Open-Circuit Stub.....	11
2.1.4 End Admittance of Microstrip Open-Circuit Stub	13
2.2 Comb-Line Antenna Array with Microstrip Open-Circuit Stubs	14
2.2.1 Microstrip Open-Circuit Stub as an Array Element.....	15
2.2.2 Comparison of Traveling Wave Array and Standing Wave Array.....	17
3 Designs of 90 and 45 Degree Standing Wave Microstrip Comb-Line Antenna Arrays	19
3.1 90 Degree Uniform Comb-Line Antenna Array	19
3.2 90 Degree Amplitude Tapered Comb-Line Antenna Array	22
3.3 45 Degree Amplitude Tapered Comb-Line Antenna Array	26
4 Measurements of 90 and 45 Degree Standing Wave Microstrip Comb-Line Antenna Arrays	29
4.1 Probe-Based Antenna Measurement Setup.....	29
4.2 Measurement Results of 90 and 45 Degree Comb-Line Antenna Arrays.....	31
4.2.1 90 Degree Amplitude Tapered Comb-Line Aray.....	31
4.2.2 45 Degree Amplitude Tapered Comb-Line Aray.....	34
5 Conclusion	37
References	39

List of Abbreviations

ACC	Adaptive Cruise Control
ADS	Advanced Design System
AiP	Antenna in Package
AoC	Antenna on Chip
AUT	Antenna Under Test
CAD	Computer-Aided Design
CMOS	Complementary Metal-Oxide-Semiconductor
CST	Computer Simulation Technology
CTA	Cross Traffic Alert
EMI	Electromagnetic Interference
eWLB	Embedded Wafer Level Ball Grid Array
FMCW	Frequency-Modulated Continuous-Wave
GaAs	Gallium Arsenide
GSG	Ground-Signal-Ground
HFSS	High Frequency Structural Simulator
HPBW	Half-Power Beamwidth
LRR	Lang Range Radar
MRR	Medium Range Radar
RCP	Redistributed Chip Package
SiGe	Silicon-Germanium
SOL	Short-Open-Load
SRR	Short Range Radar
TEM	Transverse Electromagnetic

1 Introduction

In 1904, the German inventor Christian Hülsmeyer built a device for the detection of ships in fog, which is commonly referred to as the first radar system. During World War II, radar was put into practice and under a rapid development. Nowadays, radar is also widely used in civil areas and one of the most important applications is the automotive radar system.

1.1 Overview of Automotive Radar System

As early as 1964 the use of radar system on vehicles for the prevention of collisions has been discussed [1]. In the 1970s some automotive radar prototypes were built and road tested [2]-[4]. However, at that time the high cost and large dimensions of key components were the limiting factors for commercial application. It was not until the 1990s that major automobile manufacturers and suppliers started the research on automotive radar again. Since 1992 a 24 GHz Doppler radar system developed by Eaton VORAD Technologies has been installed in 1700 Greyhound buses and it helped to reduce the accident rate by 25% [5]. In the late 90s Mercedes-Benz firstly introduced the 77GHz-radar-based DISTRONIC system [6] and other manufacturers soon followed with their own products. Today most high and middle class vehicles are equipped with radar sensors and it is safe to predict that it will be more widely available and affordable in the near future.

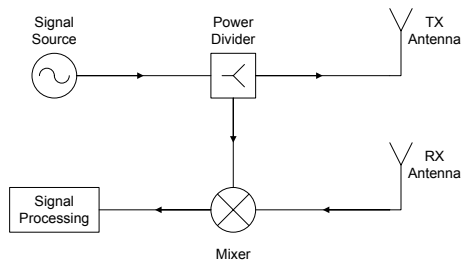


Figure 1.1 Block diagram of a frequency-modulated continuous-wave (FMCW) automotive radar

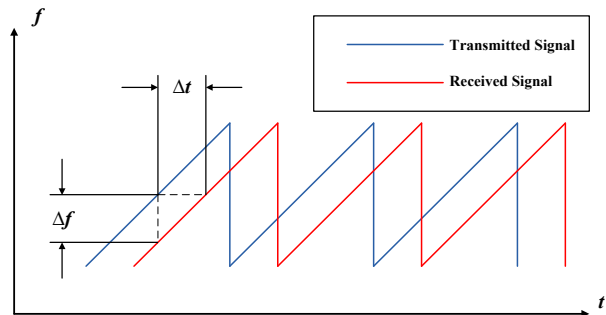


Figure 1.2 Frequency-time relationships of transmitted and received signals in FMCW radar

Figure 1.1 is the general block diagram of a frequency-modulated continuous-wave (FMCW) automotive radar, it is capable of measuring both the distance and velocity of a moving object. Assuming that a linear sawtooth frequency modulation is applied to the transmitted signal, as is shown in Figure 1.2, the time delay Δt can be calculated by

$$\Delta t = \frac{\Delta f}{k} \quad (1.1)$$

where Δf is the frequency difference between the transmitted and received signals which

could be measured from the mixer output and k is the frequency sweep rate.

The distance between the observer and target is then given by

$$d = \frac{c \cdot \Delta t}{2} \quad (1.2)$$

Here c is the speed of light in air and a factor of $1/2$ is introduced to get the one-way distance.

Two different frequency bands are available for automotive radar applications: 24 GHz and 77- GHz. The 77 GHz solution offers advantages such as smaller dimension and broader bandwidth, but also faces more challenges in design and implementation. The 77 GHz band could be divided into two subbands: 76-77 GHz and 77-81 GHz (also called 79 GHz band). The former has been approved by most countries, while the latter is only available in Europe so far but has been under discussion in other countries.

The functions of automotive radar sensors vary with their maximum ranges. Long range radar (LRR) has a narrow beam and it is usually mounted in the front grill to measure the distance of objects ahead (up to 250 m); short range radar (SRR) offers a broader beam and can be used to monitor the vicinity of a vehicle (within 30 m); between LRR and SRR, there is medium range radar (MRR) which can be installed on the front, the rear, or the side area for different applications. Detailed comparisons of the three sensor types are given in Table 1.1.

Table 1.1 Automotive radar classifications

	Maximum Range (m)	Applications
LRR	150-250	Adaptive cruise control (ACC)
MRR	60-150	Cross traffic alert (CTA), ACC
SRR	30	Blind spot detection, parking aid

The first generation of commercial automotive radar in 77 GHz was implemented in gallium arsenide (GaAs) technology [7]. Despite their excellent performance, the market share of GaAs-based products is limited by the high fabrication cost. Nowadays, most automotive radar sensors are based on silicon-germanium (SiGe) technology since it is a more cost-effective solution. As one of the main automotive semiconductor suppliers, Freescale presented its own transceiver chipset using SiGe BiCMOS technology in 2012 [8]. It consisted of a four-channel receiver and a single-channel transmitter, which covered the whole frequency range of 76-81 GHz and could be used for both LRR and SRR. Besides on-wafer measurement, the chips were also tested in redistributed chip package (RCP) and the results showed great potential for commercial applications.

In 2009, Fujitsu Laboratories reported the first 77 GHz automotive radar transceiver chip in 90 nm CMOS technology [9]; one year later, researchers from National Taiwan University published a fully integrated 77 GHz FMCW radar system in 65 nm CMOS technology [10]. The advantages of CMOS technology are the lower cost and power consumption, however, the current performances of CMOS radars are not yet comparable with their SiGe counterparts. Therefore, there is still a long way to go for CMOS automotive radars to

become competitive in consumer market.

1.2 Antennas for Automotive Radars

As an indispensable part of the radar system, antenna is a major research topic as it has huge impact on the size, cost and performance of an automotive radar sensor. The structure of antenna should be as compact as possible for easy integration into the vehicle and it must be suitable for mass production to minimize the average cost per unit. Performance-wise, it is desirable to maintain a low sidelobe level so misdetections could be avoided. All these facets pose challenges to the antenna design for automotive radars.



Figure 1.3 A 10 GHz automotive radar built in 1970s [11]



Figure 1.4 An early automotive radar with a parabolic reflector antenna [12]

In the earliest days of automotive radar, horn antenna or parabolic antenna was often chosen for the system, as shown in Figure 1.3 and 1.4 [11], [12]. However, the dimensions of these antennas are too large to fit in the vehicle and due to the high cost they are very impractical for commercial use. Breakthrough happens when the development of printed circuit technology makes planar antennas available even at millimeter wave frequencies. Since planar antennas are more compact and could be mass-produced at very low cost, they are more appropriate for commercial applications.

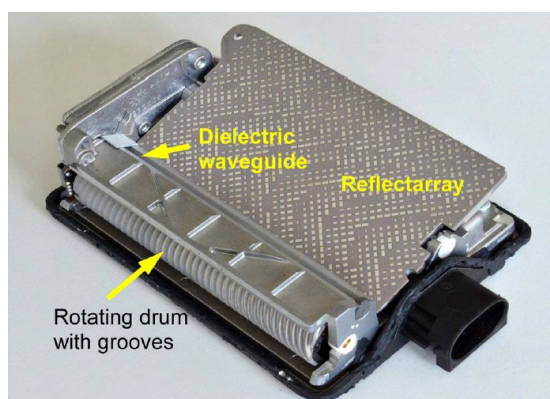


Figure 1.5 Cross section and photograph of Continental ARS 300 radar antenna [13]



Figure 1.6 Photograph of ASTYX's 77 GHz radar sensor with microstrip patch antenna arrays [14]

Two examples of antennas on currently available automotive radar products are presented below. Figure 1.5 shows the antenna used on Continental's 77 GHz radar sensor ARS 300 [13]. It consists of four parts: a rotating drum with grooves, a dielectric waveguide, a reflectarray, and a transreflector (not shown in the picture). The electromagnetic wave propagates along the dielectric waveguide is periodically perturbed by closely placed grooves of rotating drum so radiation occurs; the radiated beam is firstly reflected and then passes through the top transreflector. Beam scanning is achieved by rotation of the drum and auto-alignment could be performed by tilting the reflectarray. ASTYX's 77 GHz radar sensor shown in Figure 1.6 is equipped with a number of microstrip patch antenna arrays [14]. Each array is made up of several series-fed rectangular patch rows which are connected to a corporate feed network, and amplitude taper is utilized to improve the sidelobe suppression.

Because the above-mentioned off-chip antennas are implemented separately from the frontend chips, the transitions and connections in between will take up extra space and increase total cost. Since early 2000s the solutions to further antenna integration has been investigated, and new research topics such as antenna on chip (AoC) and antenna in package (AiP) have received great attention in recent years. In 2010, researchers from Bosch reported a 77 GHz radar transceiver chip with two integrated patch antennas separated by a distance of $\lambda/2$ [15]. The total chip size was $3.25 \times 3.25 \text{ mm}^2$ and a parasitic resonator was placed above each antenna to improve its performance. On the following year, A. Fischer *et al.* presented a 77 GHz folded dipole antenna in embedded wafer level ball grid array (eWLB) package [16]. The antenna was implemented on the redistribution layer and the whole package area was $6 \times 6 \text{ mm}^2$.

Despite their promising prospects, the on-chip antennas suffer from poor radiation efficiency due to the low resistivity nature of silicon substrates, and the achievable gain of AiP is limited since it is very difficult to increase the number of antenna elements within the package size. Also, both AoC and AiP face EMI issues. To meet these challenges, more effort will be put into future research.

The antenna group at Chalmers University of Technology has developed gap waveguide [17]-[19] V-band, E-band and UWB antennas for future wireless communication and automotive radar systems, e.g., slot array antennas [20], [21], horn array antenna [22] and other different UWB antennas [23]-[27]. However, these antennas have not been manufactured yet due to high costs.

1.3 Aim of the Thesis Project

The goal of this master thesis project is to build the receiving and transmitting antennas for Freescale's 77 GHz automotive radar prototype. The antennas should be optimized at 76.5 GHz as well as providing adequate performance over the 76-81 GHz frequency range. Microstrip technology is chosen for the implementation of antennas as it is an economical solution from the commercial point of view. At millimeter-wave frequencies, the gain of a single-element microstrip antenna is usually not high enough so various arrays are formed, among which rectangular patch array and comb-line array are widely used for automotive radar applications. Here the latter is selected for the sake of flexibility in polarization orientation.

The remainder of this thesis is organized as follows: Chapter 2 describes the general theory of comb-line antenna array. In Chapter 3, the design and simulation of both 90 and 45 degree comb-line arrays are discussed in detail. The measurement results and analysis are presented in Chapter 4. Finally, the thesis concludes with a summary in Chapter 5.

2 Analysis of Microstrip Comb-Line Antenna Array

2.1 Characteristics of Microstrip Open-Circuit Stub as a Radiating Element

The fundamental radiating element of a microstrip comb-line antenna array is the microstrip open-circuit stub. Therefore, it is necessary to investigate the radiation mechanism of an open-circuit stub before discussing the design of comb-line array.

2.1.1 Radiation Pattern of a Microstrip Open-Circuit Stub

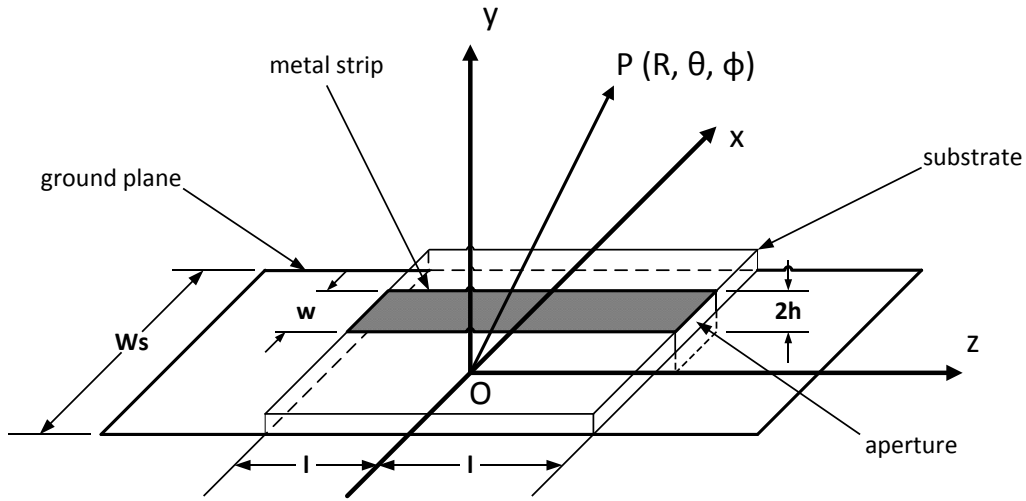


Figure 2.1 A microstrip open-circuit stub on substrate of equal length $2l$

Figure 2.1 shows an open-terminated microstrip line of length $2l$ and width w . The ground plane is placed at a height of h above the origin where h is the substrate thickness, so the image of top conductor with respect to the ground will appear in $y = 0$ plane if the conductor thickness is negligible.

The radiation pattern of above microstrip open-circuit stub can be analyzed by aperture method [28]. Assuming the microstrip line carries transverse electromagnetic (TEM) wave, so the field will be confined under the strip. When the guided wave reaches the apertures at $z = \pm l$ a part of power is radiated and the rest will be reflected. The aperture field (E, H) at $z = \pm l$ is given by

$$E = E_y \hat{y} \exp(-j\beta l)(1 + \Gamma) \quad (2.1)$$

$$H = -H_x \hat{x} \exp(-j\beta l)(1 - \Gamma) \quad (2.2)$$

in which

$$E_y = ZH_x$$

$$Z = Z_0 k/\beta$$

$$\beta = k\sqrt{\varepsilon_{\text{eff}}} = 2\pi/\lambda_g$$

where ε_{eff} is the effective permittivity of the substrate and it varies with frequency. Γ in Eq (2.1) is the reflection coefficient and it can be expressed as

$$\Gamma = |\Gamma|\exp(-j2\beta l')$$

where l' is the virtual length of the microstrip line considering the open-end effect. It reflects the capacitive loading and can be viewed as a virtual extension of the actual physical length l .

The far field E_{rad} can be expressed by the integral of E and H over aperture surface S_a

$$E_{\text{rad}} = K\hat{R}_1 \times \int_{S_a} [(\hat{n} \times E) - Z_0 \hat{R}_1 \times (\hat{n} \times H)] \exp(jk\rho_1 \cdot \hat{R}_1) da \quad (2.3)$$

where $K = -jk \exp(-jkR)/4\pi R$. ρ_1 is the vector from the coordinate origin to an arbitrary point (x', y', z') at the aperture and \hat{R}_1 is a unit vector in the direction of far-field point $P(R, \theta, \phi)$.

Substituting E and H in Eq. (2.3) with Eq. (2.1) and Eq. (2.2)

$$E_{\text{rad}} = K\hat{R}_1 \times \int_{S_a} -E_y \exp(-j\beta l) [\hat{x}\{(1 + \Gamma) + \kappa\sqrt{\varepsilon_{\text{eff}}}\cos\theta(1 - \Gamma)\} \\ - \hat{z}\cos\phi\sin\theta\kappa\sqrt{\varepsilon_{\text{eff}}}(1 - \Gamma)] \exp(jk\rho_1 \cdot \hat{R}_1) da \quad (2.4)$$

then put $\rho_1 = x'\hat{x} + y'\hat{y} + z'\hat{z}$ and $\hat{R}_1 = \cos\phi\sin\theta\hat{x} + \sin\phi\sin\theta\hat{y} + \cos\theta\hat{z}$ into the equation above

$$E_{\text{rad}} = \exp(jk\cos\theta - \beta)l\hat{R}_1 \times \\ [\hat{x}\{(1 + \Gamma) + \kappa\sqrt{\varepsilon_{\text{eff}}}\cos\theta(1 - \Gamma)\} \\ - \hat{z}\cos\phi\sin\theta\kappa\sqrt{\varepsilon_{\text{eff}}}(1 - \Gamma)]I(\theta, \phi) \quad (2.5)$$

where

$$I(\theta, \phi) = -E_y K \int_{x'=0}^W \int_{y'=0}^{2h} \exp(jk(x'\cos\phi\sin\theta + y'\sin\phi\sin\theta)) dx' dy' \quad (2.6)$$

$$= -E_y K 2hw \frac{\sin\left(\frac{kw}{2} \cdot \cos\phi \sin\theta\right) \sin(kh \sin\phi \sin\theta)}{\frac{kw}{2} \cdot \cos\phi \sin\theta \quad kh \sin\phi \sin\theta} \Psi$$

In Eq. (2.6), $\Psi = \exp\left\{jk \sin\theta \left(\frac{w}{2} \cos\phi + h \sin\phi\right)\right\}$ exists because the stub is positioned asymmetrically with respect to the origin and it will not affect the radiation pattern.

The far field radiation patterns of aperture 1 are

$$E_{\theta I} = I(\theta, \phi) \left\{ (1 + \kappa \sqrt{\epsilon_{\text{eff}}} \cos\theta) \exp(j\zeta) + |\Gamma| (1 - \kappa \sqrt{\epsilon_{\text{eff}}} \cos\theta) \exp(j\xi) \right\} \sin\phi \quad (2.7)$$

$$E_{\phi I} = I(\theta, \phi) \left\{ (\cos\theta + \kappa \sqrt{\epsilon_{\text{eff}}}) \exp(j\zeta) + |\Gamma| (\cos\theta - \kappa \sqrt{\epsilon_{\text{eff}}}) \exp(j\xi) \right\} \cos\phi \quad (2.8)$$

where

$$\zeta = k(\cos\theta - \sqrt{\epsilon_{\text{eff}}})l$$

$$\xi = k(\cos\theta - \kappa \sqrt{\epsilon_{\text{eff}}})l - 2\beta l'$$

Since w and h are much smaller than the wavelength λ_0 ,

$$\frac{\sin\left(\frac{kw}{2} \cdot \cos\phi \sin\theta\right) \sin(kh \sin\phi \sin\theta)}{\frac{kw}{2} \cdot \cos\phi \sin\theta \quad kh \sin\phi \sin\theta} \approx 1$$

is valid for any values of θ and ϕ in Eq. (2.6); besides, $|\Gamma|$ is also close to unity. So Eq. (2.7) and (2.8) can be simplified to

$$|E_{\theta I}|^2 \approx 1, \phi = \pi/2 \quad (2.9)$$

$$|E_{\phi I}|^2 \sim \cos^2\theta, \phi = 0 \quad (2.10)$$

which are equivalent to the radiation patterns of a Hertzian dipole placed along the x axis in the xz plane at the end of the stub.

2.1.2 Impact of Substrate Surface Waves

At high frequencies, the unwanted effects due to surface waves in the substrate will become non-neglectable. Therefore, it is of great importance to analyze the impact of substrate surface waves on the microstrip open-circuit stub radiation characteristics.

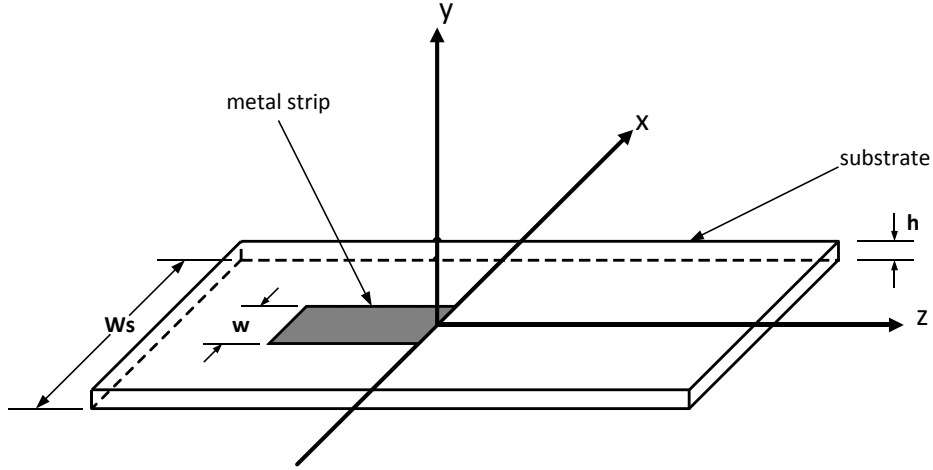


Figure 2.2 A microstrip configuration where substrate reaches beyond top conductor

Under the previous assumption, the ends of open-circuit stub and substrate lie in the same aperture plane. However, in reality the substrate will usually extend beyond the metal strip, as is shown in Figure 2.2. Assuming the substrate is infinitely long along the z -axis and the open termination is located at $z = 0$, the portion T of incident power P transformed into surface wave power P_s can be estimated by

$$T = \frac{1}{16P_s P} \left| \int_{S_a} (E_s \times H - E \times H_s) \cdot \hat{z} da \right|^2 \quad (2.11)$$

where (E, H) and (E_s, H_s) represent the incident TEM wave field and the surface wave field, respectively; the aperture S_a is specified by $-w/2 \leq x \leq w/2, 0 \leq y \leq h$ at $z = 0$.

When $z > 0$, the substrate and its image with respect to the ground can be viewed as a rectangular dielectric rod waveguide [29]. Therefore, the surface wave field in the substrate can be approximated by E_{01}^y waveguide mode with a taper $\gamma(x)$

$$H_s = \begin{cases} B \cos(k_2 y) \exp(+j\beta_s z) \gamma(x) \hat{x}, & 0 \leq y \leq h \\ A \exp[-p_1(y-h) + j\beta_s z] \gamma(x) \hat{x}, & h \leq y \leq \infty \end{cases} \quad (2.12)$$

where

$$\gamma(x) = \cos(\pi x / w_s)$$

$$\beta_s^2 = \epsilon_r k^2 - k_2^2 = k^2 + p_1^2 = (2\pi / \lambda_{gs})^2$$

$$A = B \cos(k_2 h)$$

The values of p_1 and k_2 can be obtained by solving following equations [30]

$$\begin{cases} \varepsilon_r p_1 h = k_2 h \tan(k_2 h) \\ (p_1 h)^2 + (k_2 h)^2 = (\varepsilon_r - 1)(kh)^2 \end{cases} \quad (2.13)$$

Correspondingly,

$$E_s = \begin{cases} \frac{\beta_s}{\omega \varepsilon_0 \varepsilon_r} B \cos(k_2 y) \exp(+j\beta_s z) \gamma(x) \hat{y}, 0 \leq y \leq h \\ \frac{\beta_s}{\omega \varepsilon_0} A \exp[-p_1(y-h) + j\beta_s z] \gamma(x) \hat{y}, h \leq y \leq \infty \end{cases} \quad (2.14)$$

Substituting Eq. (2.1), (2.2), (2.12) and Eq. (2.14) into Eq. (2.11)

$$T = \frac{w}{w_s F} \left[\left(k \sqrt{\frac{\varepsilon_r}{\kappa \beta \beta_s}} + \frac{1}{k} \sqrt{\frac{\kappa \beta \beta_s}{\varepsilon_r}} \right) \left\{ \frac{\sin(k_2 h)}{k_2 h} \right\} \right]^2 \quad (2.15)$$

where

$$F = \left\{ 1 + \frac{\sin(2k_2 h)}{2k_2 h} [(1 + \varepsilon_r^2 \cot^2(k_2 h))] \right\}$$

2.1.3 Improved Analysis of Microstrip Open-Circuit Stub

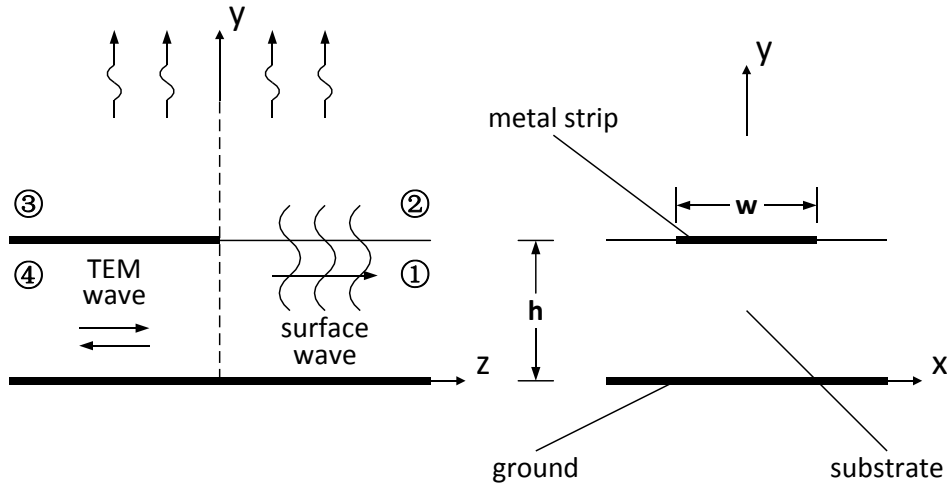


Figure 2.3 Cross sections of a microstrip open-circuit stub

Eq. (2.15) is reasonably accurate when the value of w/w_s is not much less than unity, but that is hardly the case in reality. Figure 2.3 illustrates a more practical configuration where the substrate is much wider than the stub thus can be considered infinitely large for simplicity's sake.

The field distributions of above configuration are analyzed in four regions. In region 1 and 2, the fields are characterized by the electric vector potential F and magnetic vector potential A as follows:

$$\begin{cases} F_1 = C_1 \sin(k_{y1}y) \cos(k_{x1}x) \exp(-j\beta z) \hat{z} \\ A_1 = C_2 \cos(k_{y1}y) \sin(k_{x1}x) \exp(-j\beta z) \hat{z} \end{cases} \quad (2.16)$$

$$\begin{cases} F_2 = [C_3 \sin(k_{y2}y) + C_4 \cos(k_{y2}y)] \cos(k_{x2}x) \exp(-j\beta z) \hat{z} \\ A_2 = [C_5 \sin(k_{y2}y) + C_6 \cos(k_{y2}y)] \sin(k_{x2}x) \exp(-j\beta z) \hat{z} \end{cases} \quad (2.17)$$

where

$$\begin{cases} k_{x1}^2 + k_{y1}^2 = k_0^2 \epsilon_r \mu_r - \beta^2 \\ k_{x2}^2 + k_{y2}^2 = k_0^2 - \beta^2 \end{cases}$$

Similarly, the electric and magnetic vector potentials of the surface waves in region 1 and 2 can be expressed as

$$\begin{cases} F_{1s} = C_{1s} \sin(k_{y1}y) \cos(k_x x) \exp(-j\beta z) \hat{z} \\ A_{1s} = C_{2s} \cos(k_{y1}y) \sin(k_x x) \exp(-j\beta z) \hat{z} \end{cases} \quad (2.18)$$

$$\begin{cases} F_{2s} = C_{3s} \exp(-k_{y2}(y-h)) \cos(k_x x) \exp(-j\beta z) \hat{z} \\ A_{2s} = C_{4s} \exp(-k_{y2}(y-h)) \sin(k_x x) \exp(-j\beta z) \hat{z} \end{cases} \quad (2.19)$$

where

$$\begin{cases} k_{y1}^2 = k^2 \epsilon_r - (\beta^2 + k_x^2) \\ k_{y2}^2 = (\beta^2 + k_x^2) - k^2 \end{cases}$$

Therefore, the electric and magnetic fields in region 1 and 2 can be calculated by

$$\begin{cases} E_i = \nabla(\nabla \cdot F_i) + k^2 \epsilon_i \mu_i F_i - j\omega \mu_0 \mu_i \nabla \times A_i \\ H_i = j\omega \epsilon_0 \epsilon_i \nabla \times F_i + \nabla(\nabla \cdot A_i) + k^2 \epsilon_i \mu_i A_i \end{cases} ; i = 1, 2 \quad (2.20)$$

the full solutions are given in [31].

In region 4, the fields exist in TEM mode:

$$\begin{cases} E_y = C_t(\exp(-j\beta_m z) + \Gamma \exp(j\beta_m z)) \\ H_x = -\sqrt{\frac{\epsilon_{\text{eff}}\epsilon_0}{\mu_0}} C_t(\exp(-j\beta_m z) - \Gamma \exp(j\beta_m z)) \end{cases} \quad (2.21)$$

2.1.4 End Admittance of Microstrip Open-Circuit Stub

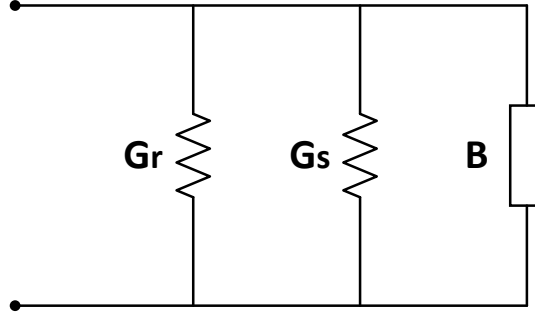


Figure 2.4 Equivalent circuit of a microstrip open-circuit stub

As depicted in Figure 2.4, the terminal admittance of a open stub consists of three parts: susceptance B , radiation conductance G_r , and G_s which represents the existence of surface waves. The expressions of G_r , B , and G_s in integral form are given below [31]

$$G_r Z_0 = \frac{1}{2} \int_0^{\pi/2} \int_0^{\pi/2} \frac{8[k^2 \epsilon_r^2 m k_{y1}^2 + \beta^2 k_x^2 g + 2\omega \epsilon_0 \epsilon_r n \beta k_x k_{y1}] f_e(A)}{\pi^2 \omega \epsilon_0 \sin(\alpha) k h w_e (g m \mu_0 / \epsilon_0 - n^2) \sqrt{(\epsilon_{\text{eff}} \epsilon_0 / \mu_0)}} d\gamma d\alpha \quad (2.22)$$

$$B Z_0 = \frac{8}{\pi^2} \int_0^{\infty} \int_0^{\pi/2} \frac{f_e(A) \epsilon_r^{3/2} \mu_0 m k_{y1}^2}{\cos(j\alpha) h w \epsilon_0 \left(g m \frac{\mu_0}{\epsilon_0} + |n|^2 \right)} d\gamma d\alpha \quad (2.23)$$

$$\frac{G_r}{G_s} = \frac{\cos^2(k_{y1} h) \epsilon_r k_{y1}^2}{\cos^2(k_{y1} h) \epsilon_r k_{y2}^2 + k_{y1}^2 h k_{y2}} \quad (2.24)$$

with

$$f_e(A) = \left[\frac{\sin(k_x w_e / 2) \sin(k_{y1} h)}{k_x k_{y1}} \right]^2 \quad (2.25)$$

$$g = \sin^2(k_{y1}h) \left(X^2 + \frac{T^2}{k^2} \right) + \cos^2(k_{y1}h) \varepsilon_r^2 \frac{k_{y1}^2}{k_{y2}^2} \quad (2.26)$$

$$m = \cos^2(k_{y1}h) \left(X^2 + \frac{T^2}{k^2} \right) + \sin^2(k_{y1}h) \frac{k_{y1}^2}{k_{y2}^2} \quad (2.27)$$

$$n = [\varepsilon_r \cos^2(k_{y1}h) - \sin^2(k_{y1}h)] \frac{k_{y1}}{k_{y2}} \frac{T}{\omega \varepsilon_0} \quad (2.28)$$

where

$$X = \frac{k^2 \varepsilon_r - \beta^2}{k^2 - \beta^2} \quad (2.29)$$

$$T = \frac{\beta k_x k^2 (\varepsilon_r - 1)}{(k^2 - \beta^2) k_{y2}} \quad (2.30)$$

In Eq (2.22) – (2.30), if β is real, for $0 \leq \alpha \leq \pi/2$, $0 \leq \gamma \leq \pi/2$

$$\begin{cases} k_x = k \sin \alpha \cos \gamma \\ k_{y2} = k \sin \alpha \sin \gamma \\ \beta = k \cos \alpha \end{cases}$$

if β is imaginary, for $0 \leq \gamma \leq \pi/2$, $0 \leq \alpha < \infty$

$$\begin{cases} k_x = k \cos(j\alpha) \cos \gamma \\ k_{y2} = k \cos(j\alpha) \sin \gamma \\ \beta = k \sin(j\alpha) \end{cases}$$

2.2 Comb-Line Antenna Array with Microstrip Open-Circuit Stubs



Figure 2.5 A microstrip comb-line antenna array composed of open-circuit stubs

Microstrip open-circuit stubs discussed in the previous section can serve as radiating elements in an antenna array. In Figure 2.5, a comb-line array is formed by connecting a number of open stubs with a feed line. The detailed analysis of comb-line antenna array will be presented in this section.

2.2.1 Microstrip Open-Circuit Stub as an Array Element

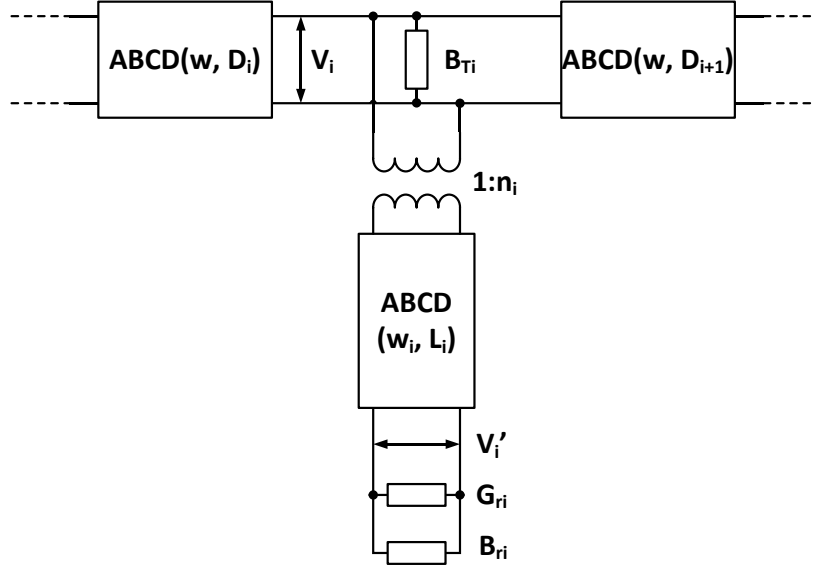


Figure 2.6 Equivalent circuit of a T-junction in microstrip comb-line antenna array

The comb-line antenna array in Figure 2.5 can be viewed as a combination of many T-junctions. Figure 2.6 depicts the equivalent circuit of a T-junction which includes a transformer with ratio n_i and a susceptance jB_{Ti} . Feedline segments and open stub around the T-junction are denoted by respective $ABCD$ matrices, and radiation of the stub is represented by the end admittance $Y_{ri} = G_{ri} + jB_{ri}$.

For the i th stub of width w_i and length L_i , the $ABCD$ matrix is given by

$$\begin{bmatrix} A & B \\ C & D \end{bmatrix}_{TL,i} = \begin{bmatrix} \cosh\{(\alpha_i + j\beta_i)L'_i\} & Z_i \sinh\{(\alpha_i + j\beta_i)L'_i\} \\ \frac{1}{Z_i} \sinh\{(\alpha_i + j\beta_i)L'_i\} & \cosh\{(\alpha_i + j\beta_i)L'_i\} \end{bmatrix} \quad (2.31)$$

where $\gamma_i = \alpha_i + j\beta_i$ is the propagation constant and Z_i is the characteristic impedance, L'_i is the effective length of the stub which is slightly longer than the physical length L_i .

The $ABCD$ matrices of the transformer and radiation admittance Y_{ri} are

$$\begin{bmatrix} A & B \\ C & D \end{bmatrix}_{transformer,i} = \begin{bmatrix} 1 & 0 \\ n_i & n_i \end{bmatrix} \quad (2.32)$$

$$\begin{bmatrix} A & B \\ C & D \end{bmatrix}_{Y_{ri}} = \begin{bmatrix} 1 & 0 \\ G_{ri} + jB_{ri} & 1 \end{bmatrix} \quad (2.33)$$

By applying the cascade rule, the total $ABCD$ matrix can be calculated

$$\begin{aligned} \begin{bmatrix} A & B \\ C & D \end{bmatrix}_{total,i} &= \begin{bmatrix} A & B \\ C & D \end{bmatrix}_{transformer,i} \begin{bmatrix} A & B \\ C & D \end{bmatrix}_{TL,i} \begin{bmatrix} A & B \\ C & D \end{bmatrix}_{Y_{ri}} \\ &= \begin{bmatrix} \frac{1}{n_i} [\cosh\{(\alpha_i + j\beta_i)L'_i\} + Z_i(G_{ri} + jB_{ri})\sinh\{(\alpha_i + j\beta_i)L'_i\}] & \frac{Z_i}{n_i} \sinh\{(\alpha_i + j\beta_i)L'_i\} \\ n_i \left[\frac{1}{Z_i} \sinh\{(\alpha_i + j\beta_i)L'_i\} + (G_{ri} + jB_{ri})\cosh\{(\alpha_i + j\beta_i)L'_i\} \right] & n_i \cosh\{(\alpha_i + j\beta_i)L'_i\} \end{bmatrix} \end{aligned} \quad (2.34)$$

Then the voltage at the end of the i th stub V'_i and the input admittance seen from the i th junction Y'_{ri} can be derived as follows:

$$V'_i = \frac{V_i}{A_{stub,i}} \quad (2.35)$$

$$Y'_{ri} = \frac{C_{stub,i}}{A_{stub,i}} \quad (2.36)$$

where

$$\begin{aligned} A_{stub,i} &= \frac{1}{n_i} \{ [\cosh(\alpha_i L'_i) \cos(\beta_i L'_i) + Z_i G_{ri} \sinh(\alpha_i L'_i) \cos(\beta_i L'_i) \\ &\quad - Z_i B_{ri} \cosh(\alpha_i L'_i) \sin(\beta_i L'_i)] \\ &\quad + j \{ \sinh(\alpha_i L'_i) \sin(\beta_i L'_i) + Z_i G_{ri} \cosh(\alpha_i L'_i) \sin(\beta_i L'_i) \\ &\quad + Z_i B_{ri} \sinh(\alpha_i L'_i) \cos(\beta_i L'_i) \} \} \\ C_{stub,i} &= \frac{n_i}{Z_i} \{ [\sinh(\alpha_i L'_i) \cos(\beta_i L'_i) + Z_i G_{ri} \cosh(\alpha_i L'_i) \cos(\beta_i L'_i) \\ &\quad - Z_i B_{ri} \sinh(\alpha_i L'_i) \sin(\beta_i L'_i)] \\ &\quad + j \{ \cosh(\alpha_i L'_i) \sin(\beta_i L'_i) + Z_i G_{ri} \sinh(\alpha_i L'_i) \sin(\beta_i L'_i) \\ &\quad + Z_i B_{ri} \cosh(\alpha_i L'_i) \cos(\beta_i L'_i) \} \} \end{aligned}$$

The radiated power from the i th stub is

$$P_i = V_i'^2 G_{ri} \quad (2.37)$$

Power distribution over the whole array can be controlled by adjusting individual stub width since radiation conductance G_{ri} will change with the stub width w_i .

2.2.2 Comparison of Traveling Wave Array and Standing Wave Array

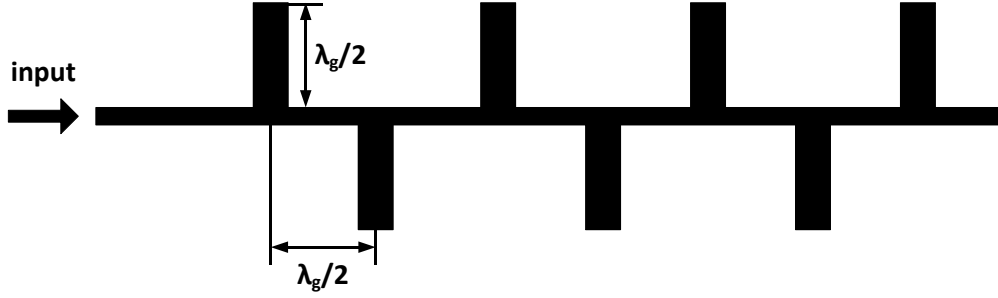


Figure 2.7 A microstrip comb-line antenna array with half-wavelength stubs and spacings

In Figure 2.5, the distance between adjacent stubs is chosen as one wavelength in order to cophase the array at desired frequency. The main disadvantage of that configuration is the existence of grating lobes and a simple solution is to place the stubs on both sides of the feedline alternatively, as illustrated in Figure 2.7. In this new arrangement, the spacing will become half a wavelength and the stubs are also half-wavelength long so the input admittance seen by the feedline is the same as the radiation admittance presented at the end of stub.

Depending on the termination, comb-line antenna arrays can be divided into two categories: traveling wave arrays and standing wave arrays. A traveling wave array is created by connecting a matching load to the end of the feedline. Consequently, the power from generator P_0 will be gradually radiated by the stubs and finally dissipated in the matching load. Thus,

$$P_0 = \sum_{i=1}^N P_i + P_L + P_{loss} \quad (2.38)$$

where $P_0 = V_0^2 G_0$, $P_L = V_L^2 G_L$, and P_{loss} is the sum of various losses in the microstrip line.

It has been proved that

$$G'_{ri} = P_i / \left(P_L + \sum_{j=1}^N P_j \right) \quad (2.39)$$

In Eq. (2.39), G'_{ri} is normalized by the feedline admittance Y .

Around a certain frequency, the relationship between radiation conductance G_{ri} and stub width w_i can be characterized by

$$G_{ri} \cong G_f (w_i / \lambda_{gi})^q \quad (2.40)$$

where G_f and q are substrate-dependent and can be determined experimentally [28].

Based on the above analysis, the design procedures of a traveling wave comb-line antenna array can be summarized as follow: first, the power P_i at each stub should be calculated for a given distribution; then the normalized radiation conductance G'_{ri} can be obtained backward (from load to generator) by Eq (2.39); once G_{ri} is known, Eq (2.40) is used to determine the stub width w_i .

In 2011, Y. Hayashi *et al.* reported a 76.5 GHz traveling wave microstrip comb-line antenna array [32]. It contained 27 elements and each element was tilted by 45 degrees for automotive radar application. To reduce unwanted reflections, a rectangular slit was placed on the feedline around every junction. At 76.5 GHz, the measured maximum gain and sidelobe level are 20.3 dBi and -17.9 dB, respectively.

A standing wave array is obtained by removing the matching load G_L so the wave will be reflected when it reaches the open end of feedline. The aperture distribution of standing wave array is also controlled by the stub width, however, it will be easier to achieve better performance without limitation of G_L .

Despite wider bandwidth and better input matching, the traveling wave array has a major disadvantage of beam squint. In order to get a broadside beam without deteriorating the matching, various reflection-canceling techniques have to be applied. Obviously, it will increase the cost and complexity of the antenna. On the other hand, the standing wave array has a broadside beam and much simpler structure, so from the budget and reliability point of view it would be a more appropriate choice for industrial applications.

In 2011, L. Zhang *et al.* presented a standing wave microstrip comb-line antenna array for 24 GHz automotive radar application [33]. To the best knowledge of the author, there is no report of standing wave comb-line array at 77GHz yet. Therefore, it is a potentially valuable research topic and this thesis project aims to fill the gap.

3 Designs of 90 and 45 Degree Standing Wave Microstrip Comb-Line Antenna Arrays

Today there are many commercial CAD (computer-aided design) software products for antenna design, among which HFSS and CST are most commonly used. Both of them can handle complicated structures and give very accurate results if set up properly. However, they may not be the optimal choice for this project because the simulation is usually very time-consuming and the modeling process can also be quite tedious.

Although not as powerful as HFSS and CST, the Momentum simulator of ADS (Advanced Design System) is also capable of performing antenna simulations. For simple planar structure such as comb-line array, Momentum can provide results with adequate accuracy in a much shorter time. Therefore, it is chosen as a more efficient solution considering the limited time for this project.

Based upon the previous discussion, the comb-line array should be realized in standing wave configuration with 45 degree polarization orientation for automotive radar application. To begin with, 90 degree linearly polarized arrays will be developed since it is the original structure and can serve as the basis for the following work.

3.1 90 Degree Uniform Comb-Line Antenna Array

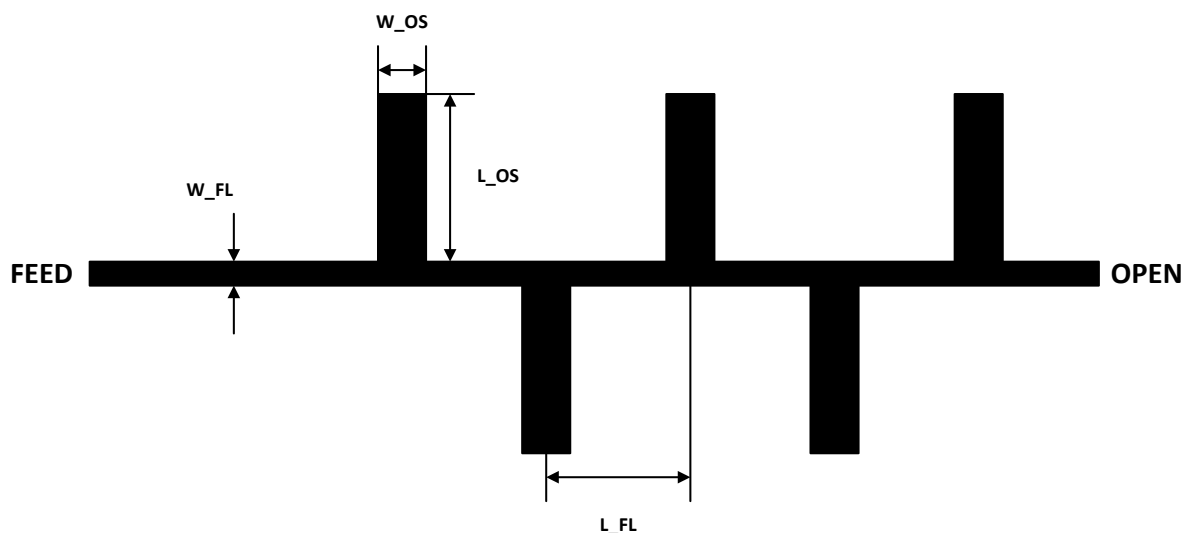


Figure 3.1 A 90 degree uniform microstrip comb-line antenna array

Figure 3.1 shows a 90 degree uniform comb-line antenna array in standing wave configuration. As discussed earlier, the length of open stub L_{OS} and the spacing between adjacent stubs L_{FL} both equal to half a wavelength; the amplitude distribution of the array is controlled by the open stub width W_{OS} . In the simplest case of uniform array, the width of each stub is the same so power will be evenly spread over the aperture.

The whole microstrip structure will be implemented on Rogers RO3003 substrate. At

76.5 GHz the relative permittivity and loss tangent of substrate are $\epsilon_r=3.2$ and $\tan \delta=0.0168$, respectively. These parameters are established experimentally since the values in datasheet are only valid for much lower frequencies.

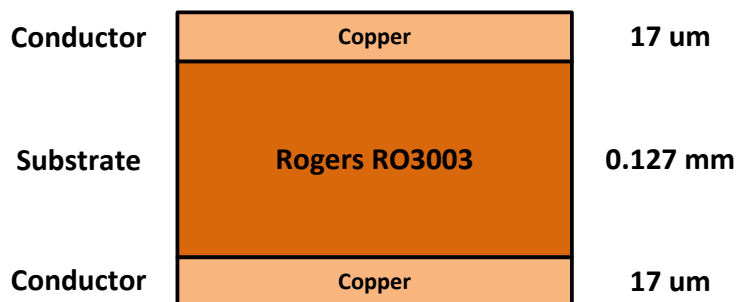


Figure 3.2 Layer stack of the antenna board

As can be seen in Figure 3.2, the substrate is sandwiched by two conductor layers. The top layer is utilized for antenna design and the bottom layer is used as ground. Due to manufacturing constraints, the realizable minimum line width is 0.10 mm and the fabrication tolerance is 0.01 mm.

The LineCalc tool of ADS can be used to calculate the electrical length and characteristic impedance of a transmission line if the physical dimensions are given, and vice versa. Therefore, after adding the substrate parameters in LineCalc, the length l and width w of a 50 ohm half-wavelength stub can be obtained as $l=1.24$ mm and $w=0.30$ mm, respectively.

In light of the above analysis, the initial dimensions of 90 degree uniform comb-line array are chosen as follows: stub width $W_{OS}=0.30$ mm, stub length $L_{OS}=1.24$ mm, feedline width $W_{FL}=0.10$ mm, and the distance between adjacent stubs $L_{FL}=1.24+0.30=1.54$ mm. The next step is to determine the number of array elements N . In order to investigate the impact of element number on antenna performance, three arrays with different values of N are created in ADS and the simulation results are compared below.

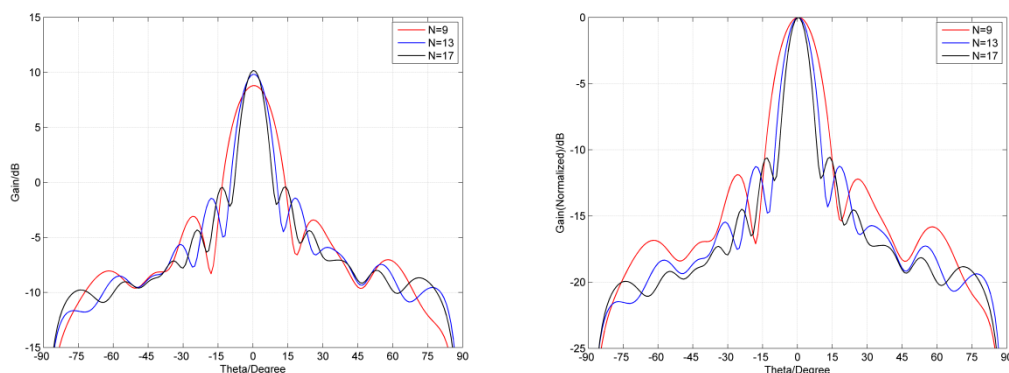


Figure 3.3 The unnormalized (left) and normalized (right) H-plane radiation patterns of 90 degree uniform comb-line arrays with 9, 13 and 17 elements.

Figure 3.3 shows the comparison of H-plane radiation pattern simulation results in ADS for 90 degree uniform comb-line antenna arrays with $N=9, 13, 17$ elements. The left figure above indicates that the beam will become sharper and the gain will be higher if more elements are utilized; however, the increasing number of elements will result in worse sidelobe suppression, as can be observed in the right figure above where each trace is normalized by its own maximum, and the bandwidth will also start shrinking. Taking all these factors into consideration, the value of $N = 13$ is selected to achieve optimum performance.

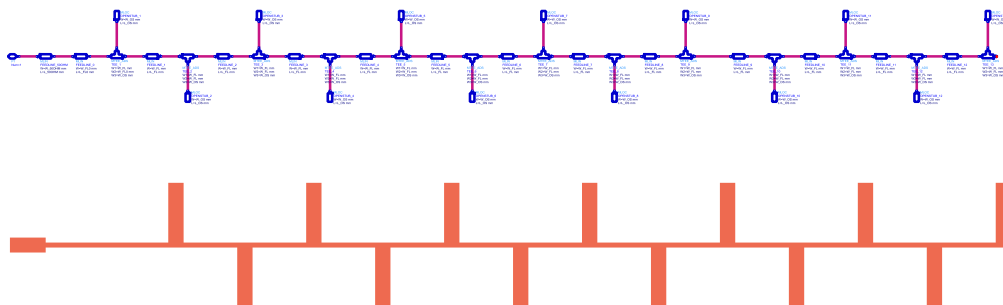


Figure 3.4 13-element 90 degree uniform microstrip comb-line antenna array in ADS schematic (top) and Momentum simulator (bottom)

The ADS schematic and layout models of the 13-element 90 degree uniform comb-line array are shown in Figure 3.4. After optimizations the final array dimensions are $W_{OS}=0.30$ mm, $L_{OS}=1.20$ mm, $W_{FL}=0.10$ mm and $L_{FL}=1.35$ mm.

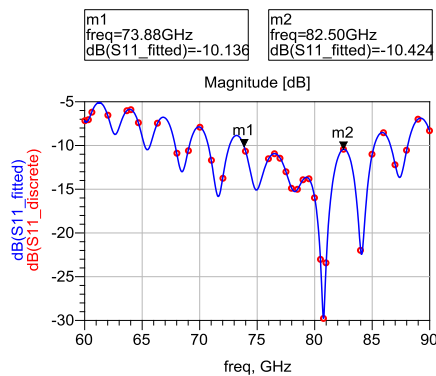


Figure 3.5 Simulated reflection coefficient of the 90 degree uniform comb-line array

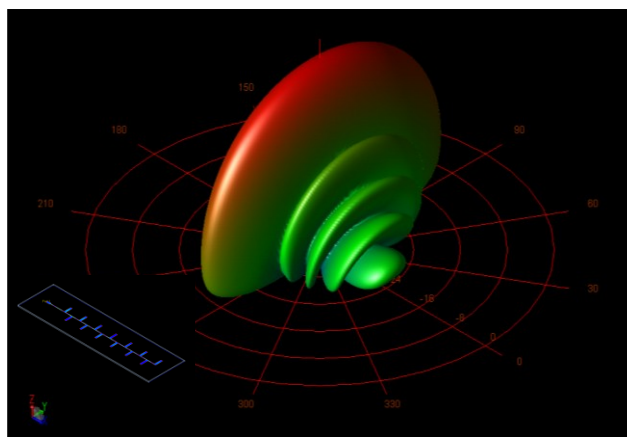


Figure 3.6 Simulated 76.5 GHz 3D radiation pattern of the 90 degree uniform comb-line array

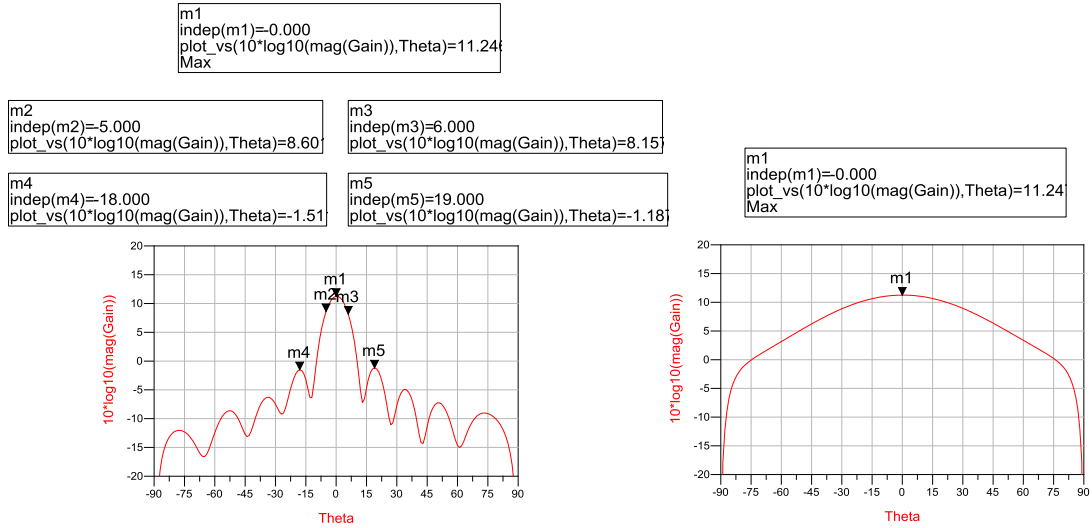


Figure 3.7 Simulated 76.5 GHz $H(xz)$ -plane (left) and $E(yz)$ -plane (right) radiation patterns of the 90 degree uniform comb-line array

Simulation results of reflection coefficient from 60 to 90 GHz and radiation patterns at 76.5 GHz are presented in Figures 3.5 through 3.7. The return loss is better than 10 dB from 73.9 to 82.5 GHz which means good impedance matching is achieved over the desired frequency range. The 3D radiation pattern in Figure 3.6 demonstrates a broadside beam with a fan-shaped mainlobe. Peak radiation occurs at $\theta = 0^\circ$ and the maximum gain is 11.24 dBi. In the $H(xz)$ -plane radiation pattern, the half-power beamwidth (HPBW) is approximately 11 degrees and the sidelobe level is -12.42 dB.

3.2 90 Degree Amplitude Tapered Comb-Line Antenna Array

It has been proven that the best sidelobe level a uniform linear array could obtain is about -13.46dB and the previous simulation result is very close to the limit. In order to achieve better sidelobe suppression, non-uniform amplitude distribution could be formed on the array by applying various amplitude tapering methods. Here Taylor distribution is selected as it offers an optimal balance between beamwidth and sidelobe level.

The radiation pattern of a Taylor weighted array exhibits the following properties: the first \bar{n} sidelobes near the mainlobe are at the same level $1/R_0$ while the rest decrease monotonically. Both parameters \bar{n} and $1/R_0$ are specified by designer. The value of \bar{n} should be carefully determined as it will influence the peak positions of amplitude distribution on the array. Generally for -25 dB sidelobe level \bar{n} should be no less than 3 [34].

To improve the sidelobe suppression, the previous uniform array will be modified with a 20 dB ($\bar{n}=3$) Taylor amplitude taper. The corresponding voltage ratio is

$$R_0 = \cosh(\pi A) = 10 \quad (3.1)$$

Thus the constant A can be calculated by

$$A = \frac{1}{\pi} \cosh^{-1}(R_0) = 0.95 \quad (3.2)$$

The scaling factor σ is given by

$$\sigma = \frac{\bar{n}}{\sqrt{A^2 + \left(\bar{n} - \frac{1}{2}\right)^2}} = 1.12 \quad (3.3)$$

and the normalized current distribution over the array can be expressed as

$$I(z') = \frac{\lambda}{l} \left[1 + 2 \sum_{p=1}^{\bar{n}-1} \text{SF}(p, A, \bar{n}) \cos\left(2\pi p \frac{z'}{l}\right) \right] \quad (3.4)$$

In the equation above, the Taylor space factor $\text{SF}(p, A, \bar{n})$ can be written as

$$\text{SF}(p, A, \bar{n}) = \begin{cases} \frac{[(\bar{n}-1)!]^2}{(\bar{n}-1+p)! (\bar{n}-1-p)!} \prod_{m=1}^{\bar{n}-1} \left[1 - \left(\frac{\pi p}{u_m}\right)^2 \right], & |p| < \bar{n} \\ 0, & |p| \geq \bar{n} \end{cases} \quad (3.5)$$

where

$$u_m = \pi \frac{l}{\lambda} \cos \theta_m = \begin{cases} \pm \pi \sigma \sqrt{A^2 + \left(m - \frac{1}{2}\right)^2}, & 1 \leq m < \bar{n} \\ \pm m\pi, & \bar{n} \leq m \leq \infty \end{cases}$$

and θ_m is the location of the m th sidelobe in the radiation pattern.

Table 3.1 Normalized current levels on the 90 degree comb-line antenna array with 20 dB ($\bar{n}=3$) Taylor amplitude taper

Element No.	1	2	3	4	5	6	7
Normalized Current	0.5256	0.5557	0.6393	0.7562	0.8765	0.9666	1.0000

The normalized currents on each stub are determined by Eq. (3.1)–(3.5) and listed in Table 3.1. Only half of the values need to be calculated since the distribution is symmetric. Once the current distribution is established, the following task is to decide the corresponding stub widths.

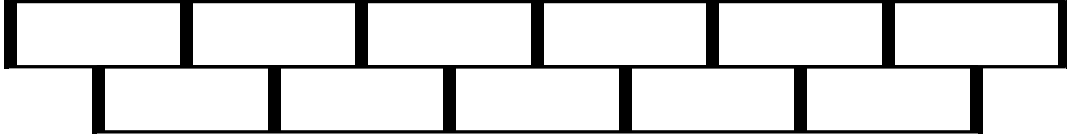


Figure 3.8 A microstrip grid antenna array with grid size of $\lambda \times 0.5\lambda$

Figure 3.8 demonstrates a microstrip grid antenna array where the size of each grid is $\lambda \times 0.5\lambda$. The main radiation elements in this array are the short sides of the grids. At the end of short sides the currents are close to zero so the long sides surrounding the array can be removed without altering the radiation pattern too much, then the grid array will be transformed to the comb-line array in Figure 3.4. Therefore, a comb-line array can be viewed as the variation of a grid array and their radiation mechanisms are very similar.

According to [33], in a microstrip grid antenna array with Taylor amplitude taper, the characteristic impedance of a short side is inversely proportional to the normalized current it carries. The same method can be applied to the design of a Taylor comb-line array. From Table 3.1, stubs at two ends of the array (No. 1 and No. 13) will carry the lowest currents, so their characteristic impedances should be the highest among all stubs. Therefore, stub No. 1 and No. 13 are assigned the minimum manufacturable line width of 0.10 mm as it corresponds to the maximum implementable characteristic impedance of 87.40 ohm, then the characteristic impedances of other stubs can be obtained by

$$Z_{0,i} = Z_{0,14-i} = \frac{I_1 Z_1}{I_i} = \frac{0.5256 \times 87.40}{I_i} = \frac{45.94}{I_i}, 2 \leq i \leq 7$$

Once the characteristic impedance is known, the stub width can be easily determined by LineCalc in ADS. Table 3.2 depicts the characteristic impedance of each array element and its corresponding stub width; the array layout in ADS is shown in Figure 3.9.

Table 3.2 Characteristic impedances and widths of open-circuit stubs in the 90 degree comb-line array with 20 dB ($\bar{n}=3$) Taylor amplitude taper

Element No.	1	2	3	4	5	6	7
Characteristic Impedance (ohm)	87.40	82.66	71.86	60.75	52.41	47.53	45.94
Stub Width (mm)	0.10	0.12	0.16	0.22	0.28	0.33	0.35

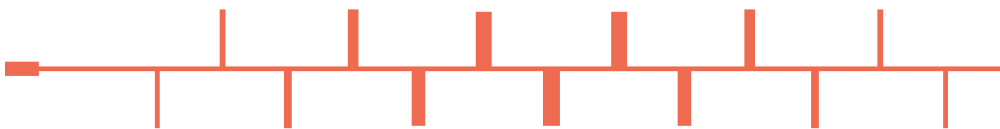


Figure 3.9 Layout of the 13-element 90 degree comb-line array with 20 dB ($\bar{n}=3$) Taylor amplitude taper

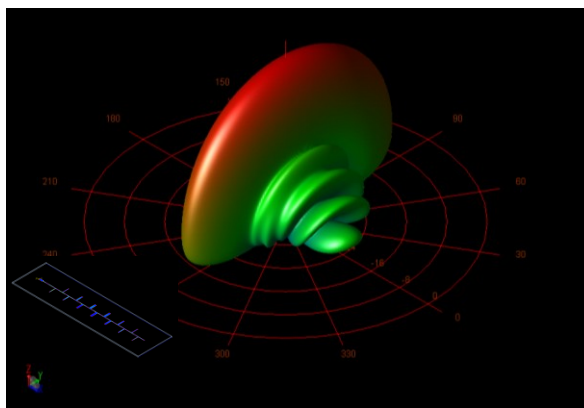
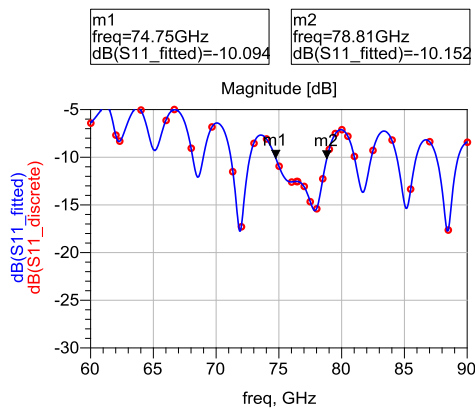


Figure 3.10 Simulated reflection coefficient of the 90 degree amplitude tapered comb-line array

Figure 3.11 Simulated 76.5 GHz 3D radiation pattern of the 90 degree amplitude tapered comb-line array

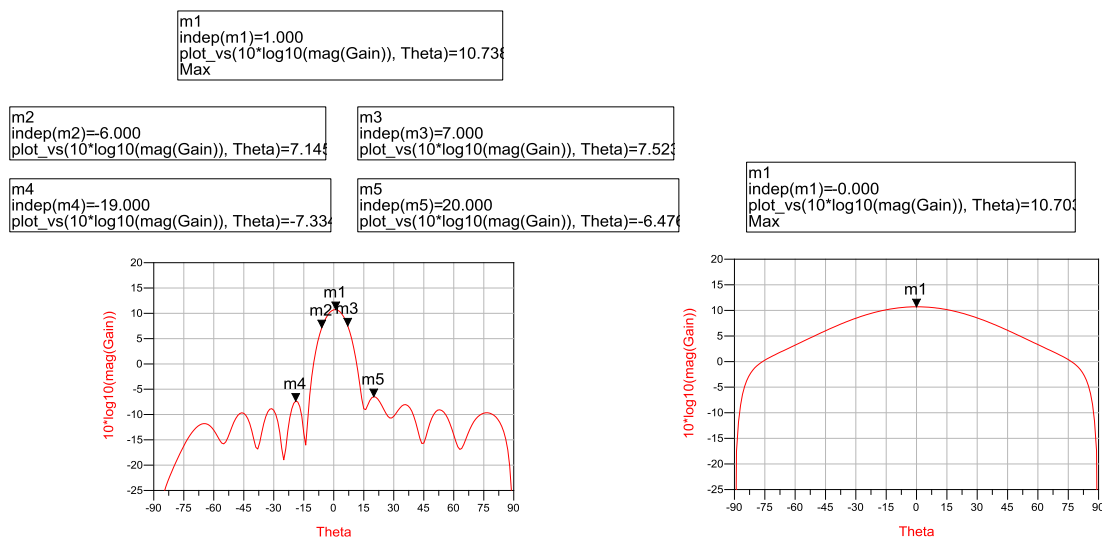


Figure 3.12 Simulated 76.5 GHz $H(xz)$ -plane (left) and $E(yz)$ -plane (right) radiation patterns of the 90 degree amplitude tapered comb-line array

Simulation results of the Taylor weighted array are displayed in Figure 3.10 through 3.12. The -10dB impedance bandwidth is from 74.7 to 78.8 GHz. As shown in the 76.5 GHz $H(xz)$ -plane radiation pattern, the gain reaches its maximum value of 10.73 dBi at $\theta = +1^\circ$, the HPBW is about 12 degrees and the sidelobe suppression is better than 17.2 dB.

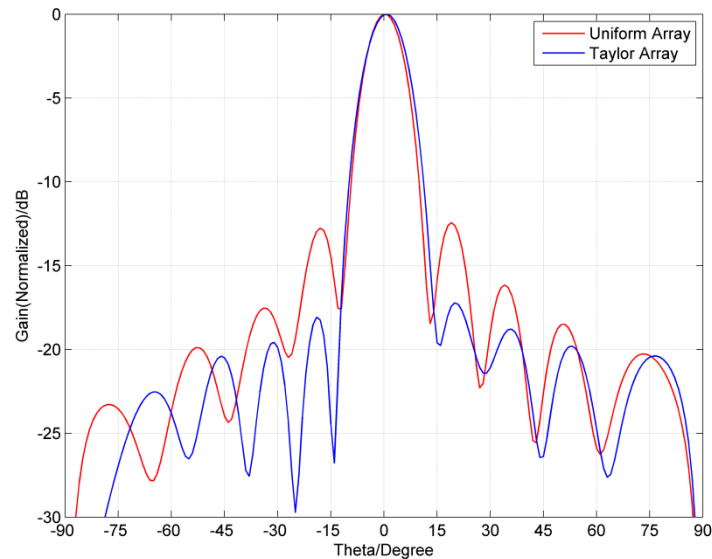


Figure 3.13 Normalized 76.5 GHz $H(xz)$ -plane radiation patterns of the 90 degree uniform array and amplitude tapered array

Figure 3.13 compares the normalized 76.5 GHz $H(xz)$ -plane radiation patterns of the previous uniform array and Taylor array. Obviously, the sidelobe suppression has been significantly improved (approximately 5 dB) after applying the amplitude taper, and the differences in the first three sidelobes' power levels of the Taylor array are much smaller than those of the uniform array, as it is expected.

3.3 45 Degree Amplitude Tapered Comb-Line Antenna Array

In the previous configurations, all open-circuit stubs are perpendicular to the main feed line so those arrays are 90 degree linearly polarized. The disadvantage of this configuration is that automotive radars equipped with such antennas cannot distinguish between the reflected signals and signals transmitted by vehicles from the opposite directions. One solution is to create a 45 degree linearly polarized array by tilting the orientation of stubs to 45 degrees, then signals from vehicles traveling in opposite directions are orthogonal (assuming 45 degree antennas are installed on both vehicles) and the interferences will be minimized.



Figure 3.14 Layout of the 13-element 45 degree comb-line array with 20 dB ($\bar{n}=3$) Taylor amplitude taper

The design principle of 45 degree comb-line antenna array is very similar to that of 90 degree array presented in previous sections, therefore it will not be described in detail here.

Figure 3.14 shows a 45 degree 13-element comb-line array with 20 dB ($\bar{n}=3$) Taylor amplitude taper. The stub widths are exactly the same as values given in Table 3.2, whereas the stub lengths are slightly shorter ($L_{OS}=1.05$ mm). The stubs are fully connected to feedline for ease of manufacturing.

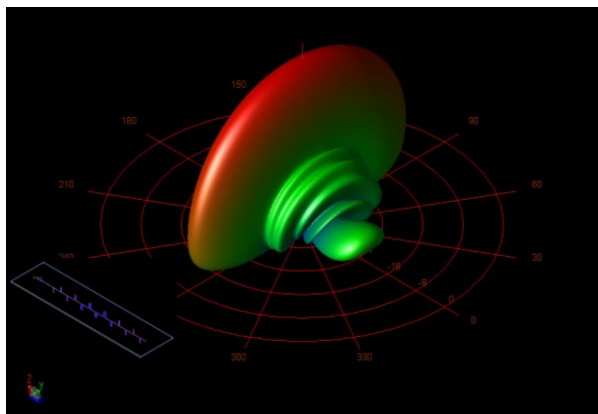
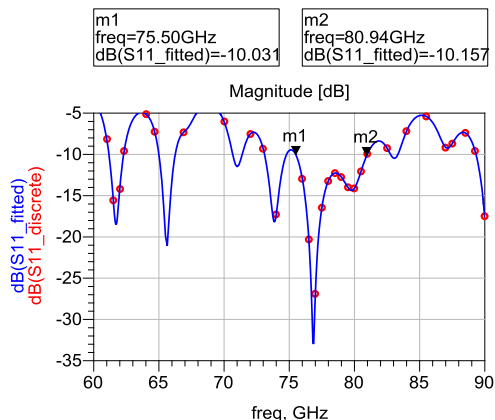


Figure 3.15 Simulated reflection coefficient of the 45 degree amplitude tapered comb-line array

Figure 3.16 Simulated 76.5 GHz 3D radiation pattern of the 45 degree amplitude tapered comb-line array

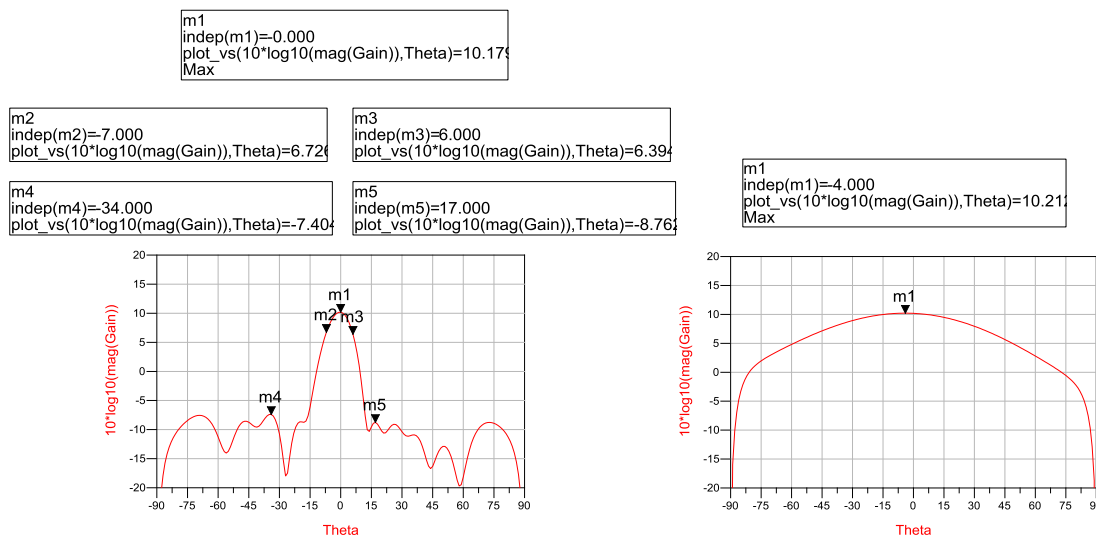


Figure 3.17 Simulated 76.5 GHz xz -plane (left) and yz -plane (right) radiation patterns of the 45 degree amplitude tapered comb-line array

Simulation results of the 45 degree amplitude tapered array are shown in Figure 3.15 through 3.17. The reflection coefficient is below -10 dB from 75.50 to 81.00 GHz. As depicted in the 76.5 GHz xz -plane radiation pattern, the beam direction is $\theta = 0^\circ$ and the HPBW is around 12 degrees; the maximum gain is 10.18 dBi and the worst sidelobe level is -17.58 dB.

It is worth noting that the orientation of radiation pattern in Figure 3.16 remains the same as Figure 3.11 even if the stubs are shifted from 90 to 45 degrees. This is due to the fact that

the radiation pattern of a half-wavelength open stub is almost omnidirectional. As illustrated in Figure 3.18, there is only very tiny difference between the top views of 90 and 45 degree patterns, and the two array factors are identical since the same arrangement of elements and amplitude taper are implemented in both arrays. Therefore, the final results are quite similar to each other.

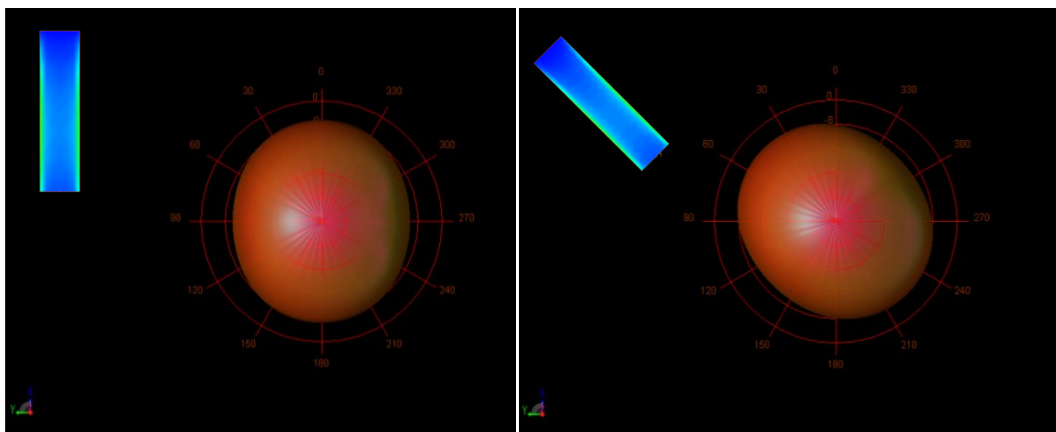


Figure 3.18 Topviews of 3D radiation patterns for a half-wavelength open-circuit stub oriented at 90 and 45 degrees

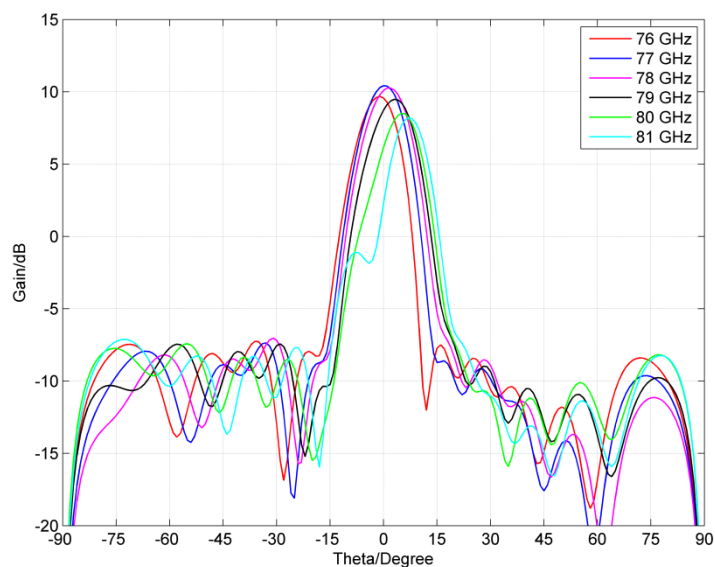


Figure 3.19 76 to 81 GHz (separated by 1 GHz) xz -plane radiation patterns of the 45 degree amplitude tapered comb-line antenna array

Figure 3.19 illustrates the xz -plane radiation patterns of the 45 degree comb-line array from 76 to 81 GHz with 1 GHz spacing. The performance is adequate up to 79 GHz but it starts to deteriorate above 80 GHz, as indicated in the figure.

4 Measurements of 90 and 45 Degree Standing Wave Microstrip Comb-Line Antenna Arrays

The traditional antenna measurement approach is to mount the antenna under test (AUT) on a rotating turntable in anechoic chamber and connect it with coaxial cable. It works fine at low frequencies when the size of antenna is larger than or comparable to the connectors. However, as frequency increases the AUT will shrink dramatically in size so it becomes much more challenging to put them together.

During the past decade, probe-based antenna measurement setups start to emerge [35]-[37]. As the name implies, in these configurations the AUT is in contact with a probe. It is less bulky than the conventional setup since those connectors and adapters can be omitted; another advantage is the probe can be placed at the exact point of interest without any transitions in-between so no de-embedding is involved. Thus, a probe-based setup is chosen for the measurements of fabricated comb-line antenna arrays.

4.1 Probe-Based Antenna Measurement Setup

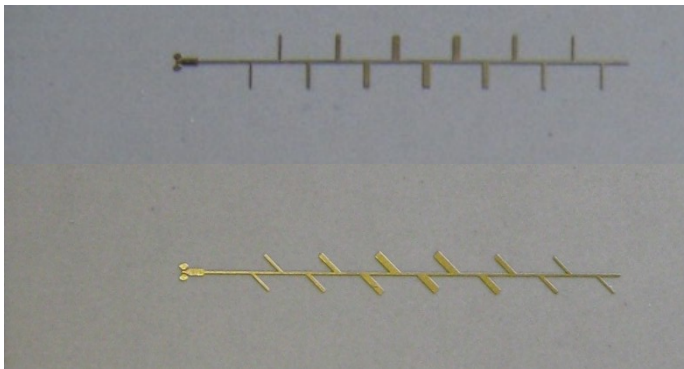


Figure 4.1 Fabricated 90 and 45 degree amplitude tapered microstrip comb-line antenna arrays

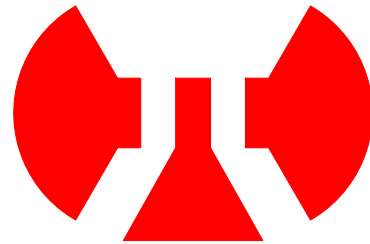


Figure 4.2 Pad footprint for ground-signal-ground (GSG) probe

Figure 4.1 demonstrates the 90 and 45 degree amplitude tapered comb-line arrays manufactured by Elekonta Marek GmbH & Co. KG. A ground-signal-ground (GSG) pad shown in Figure 4.2 is placed at the feed point of each antenna. The dimensions of 90 and 45 degree arrays are $20.7 \times 2.5 \text{ mm}^2$ and $20.5 \times 2.0 \text{ mm}^2$, respectively.

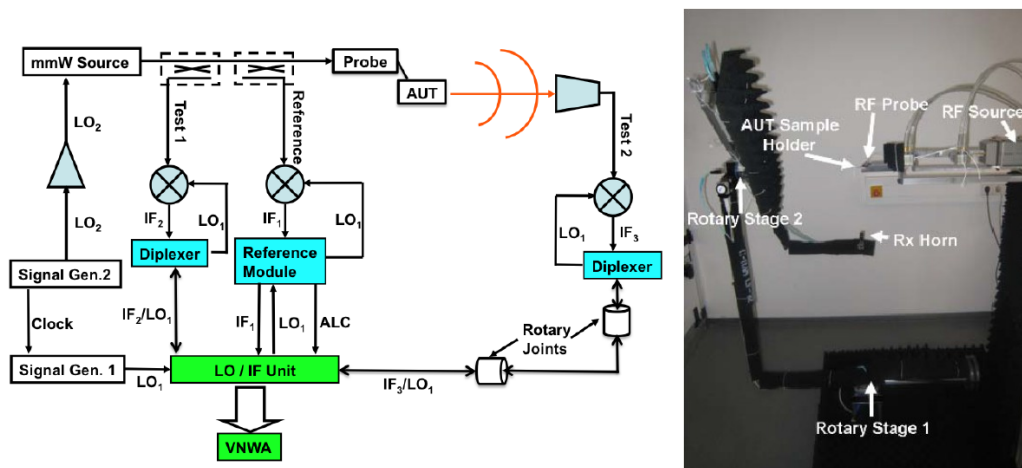


Figure 4.3 Block diagram (left) and photograph (right) of the probe-based antenna measurement setup [38]

The measurements of both antennas are performed at Karlsruhe Institute of Technology. Block diagram and photograph of the measurement setup are shown in Figure 4.3 [38]. It is capable of performing S-parameters and radiation patterns measurement in V- or W-band, with extender module the maximum operating frequency can even be pushed up to 325 GHz [39].

In this setup the AUT acts as a transmitting antenna and the receiving antenna is a standard gain horn. As shown in the picture above, the AUT is touched by a coplanar probe. A small piece of low loss, low permittivity foam is placed under the antenna substrate and the surrounded objects are also covered by radiation absorbent material. The probe is very fragile so it needs to stay stationary to avoid damage and the receiving horn antenna will be rotating around AUT instead. The horn is mounted on a vertically rotating arm which is attached to another horizontally rotating arm and both arms are driven by motorized rotation stages. 3D radiation pattern of AUT can be obtained as the horn antenna will move over an AUT-centered sphere. Both co- and cross-polarization can be measured by altering orientation of the horn.

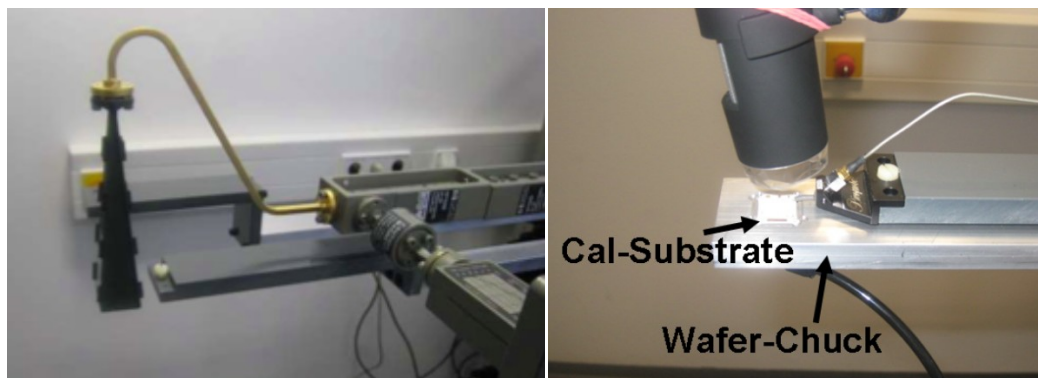


Figure 4.4 Gain calibration (left) and short-open-load (SOL) calibration (right) of the setup [38]

Two types of calibration should be performed on the probe-based setup prior to the measurement, as demonstrated in Figure 4.4. The gain calibration is done by substituting the AUT with another standard gain horn antenna which is connected to a bent waveguide to ensure its location is exactly the same as the AUT's. In order to measure the antenna impedance, the port reference plane is positioned at the probe and a short-open-load (SOL) calibration is conducted by replacing the AUT with a calibration substrate, then the gain of probe can be determined from the measured reflection coefficients of short, open and load standards. Usually the gain calibration is done first since it will lead to more adjustment on the initial setup and it also has longer validity period. Both calibrations are fully managed by custom-developed software.

4.2 Measurement Results of 90 and 45 Degree Comb-Line Antenna Arrays

4.2.1 90 Degree Amplitude Tapered Comb-Line Array

In the probe-based setup from the previous section, the AUT and reference horn antenna are separated by a distance of 60 cm. In order to properly measure the far-field radiation patterns, it is critical that the reference horn must be located in the far-field region of the AUT.

The far-field distance of an antenna can be calculated by

$$R = \frac{2D^2}{\lambda} \quad (4.1)$$

where D is the maximum dimension of the antenna and λ is the wavelength. Eq. (4.1) is only valid if $D > \lambda$.

For the 90 degree amplitude tapered comb-line antenna array, D is the array length of 20.7 mm and the free-space wavelength at 76.5 GHz is $\lambda = c_0/f = 3.92$ mm. The far-field distance is $R = 2D^2/\lambda = 21.85$ cm which is obviously smaller than the distance between the horn antenna and AUT so the precondition for measurement is satisfied.

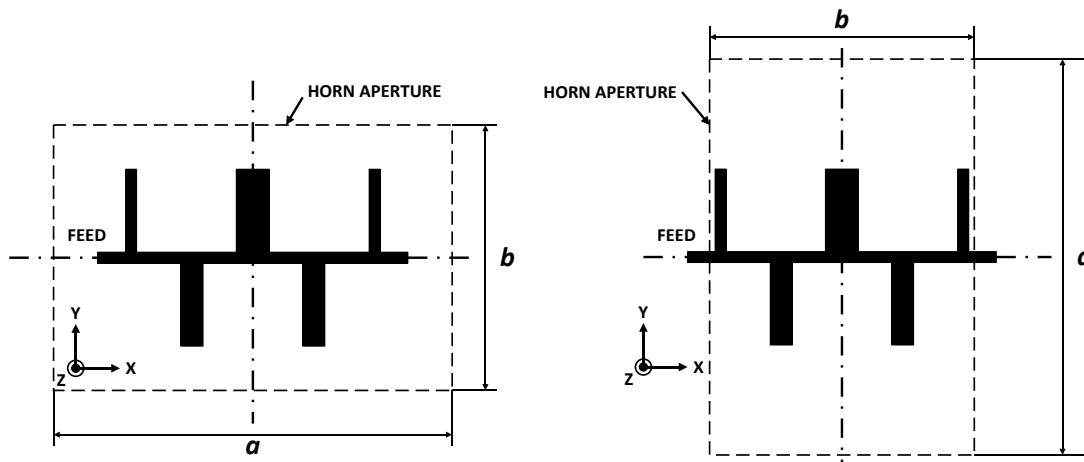


Figure 4.5 Orientations of reference horn antenna with respect to AUT for co-polarization (left) and cross-polarization (right) radiation pattern measurements of 90 degree comb-line array

Figure 4.5 illustrates the relative orientations of 90 degree comb-line antenna array and receiving horn antenna for both co- and cross-polarization measurements. With careful alignment, the centers of two antennas are coincident with each other. Once co-polarization measurement is done, the horn antenna is rotated by 90 degrees for cross-polarization measurement.

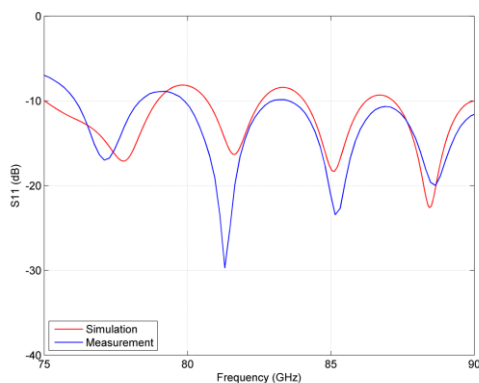


Figure 4.6 Measured and simulated reflection coefficient of the 90 degree amplitude tapered comb-line array

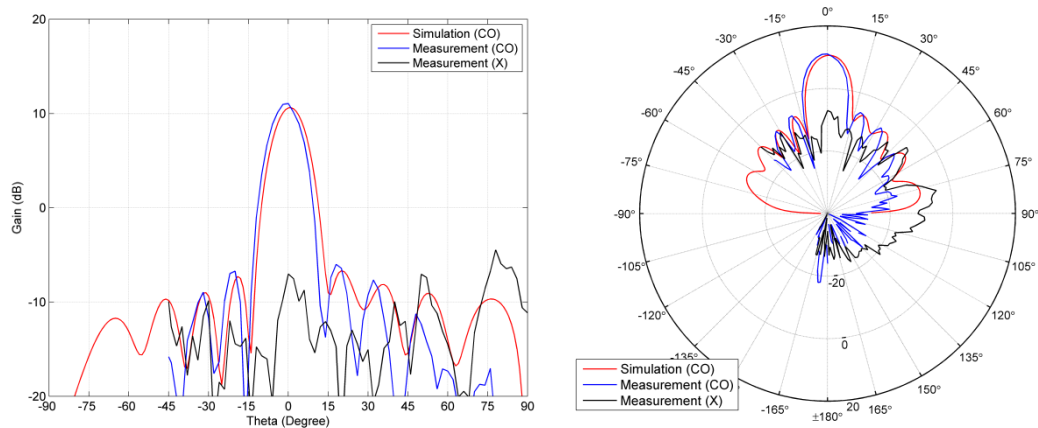


Figure 4.7 Measured and simulated 76.5 GHz $H(xz)$ -plane co-polarization and cross-polarization radiation patterns of the 90 degree amplitude tapered comb-line array plotted in Cartesian coordinate (left) and polar coordinate (right)

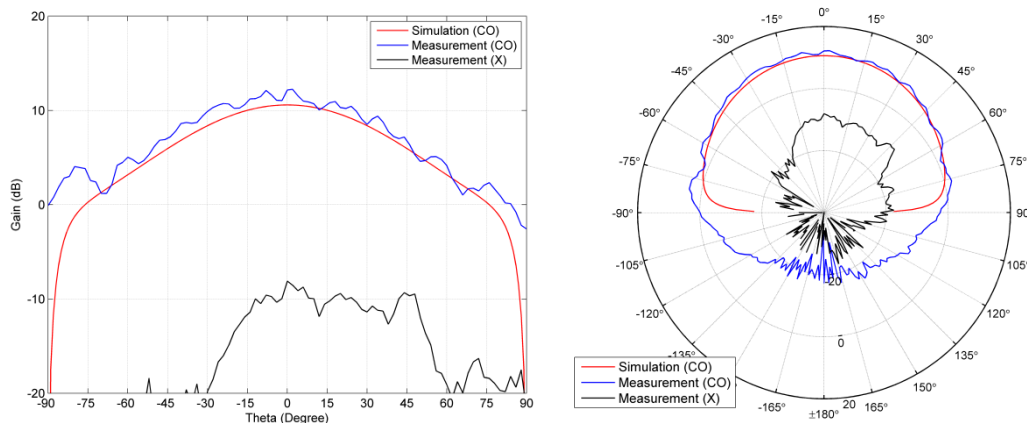


Figure 4.8 Measured and simulated 76.5 GHz $E(yz)$ -plane co-polarization and cross-polarization radiation patterns of the 90 degree amplitude tapered comb-line array plotted in Cartesian coordinate (left) and polar coordinate (right)

The comparisons between simulation and measurement results are presented in the figures above. Figure 4.6 shows the measured return loss which is basically better than 10 dB beyond 76 GHz. The $H(xz)$ - and $E(yz)$ -plane radiation patterns at 76.5 GHz are given in Figure 4.7 and 4.8, respectively. In the measured $H(xz)$ -plane co-polarization radiation pattern, the maximum gain is 11.06 dBi and the direction of maximum radiation is $\theta = 0^\circ$; the HPBW is approximately 12 degrees and the sidelobe suppression is better than 17 dB. The cross-polarization levels fluctuate around -10 dB in both planes. Overall, good agreements between simulation and measurement results of the S-parameters and co-polarization radiation patterns has been observed, whereas no comparison can be made for the cross-polarization patterns since it is not available in ADS simulations.

It is noteworthy that a blind region exists in the measured $H(xz)$ -plane radiation patterns from -150° to -45° where no measurement data is available. The reason is that $H(xz)$ -plane contains the feedline which means the probe should also lie in the same plane, therefore, the movement of rotating arm must be restricted, otherwise collision will happen. On the other hand, $E(yz)$ -plane is perpendicular to the feedline and the rotation path is obstacle-free so it does not suffer from this problem.

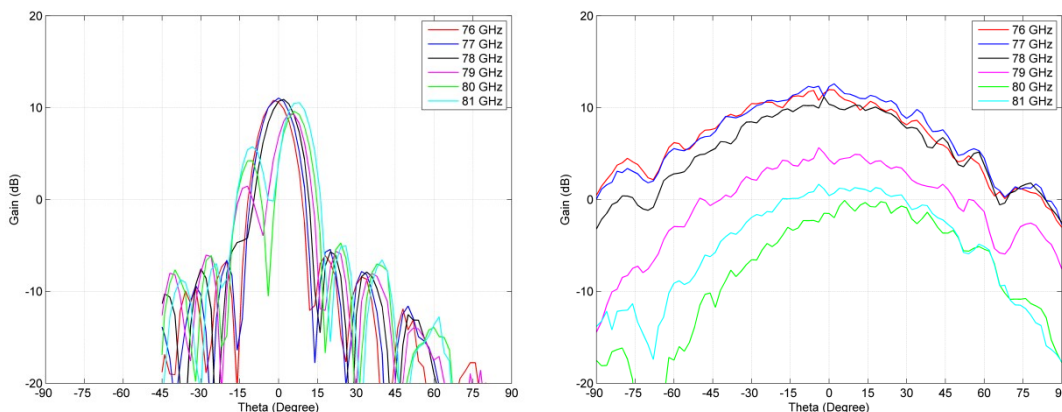


Figure 4.9 Measured $H(xz)$ -plane and $E(yz)$ -plane co-polarization radiation patterns of the 90 degree amplitude tapered comb-line array from 76 to 81 GHz (separated by 1 GHz)

Figure 4.9 illustrates the co-polarization radiation patterns of both $H(xz)$ - and $E(yz)$ -planes from 76 to 81 GHz in 1 GHz step. The performances are fairly consistent between 76 and 78 GHz but significant deteriorations arise for frequencies over 78 GHz.

4.2.2 45 Degree Amplitude Tapered Comb-Line Array

The far-field distance of 45 degree amplitude tapered comb-line antenna array at 76.5 GHz can be determined by applying $D=20.5$ mm and $\lambda=3.92$ mm to Eq. (4.1). The result of $R = 2D^2/\lambda = 21.43$ cm is smaller than the 60 cm distance from AUT to receiving horn antenna so the far-field condition is fulfilled for the radiation pattern measurements.

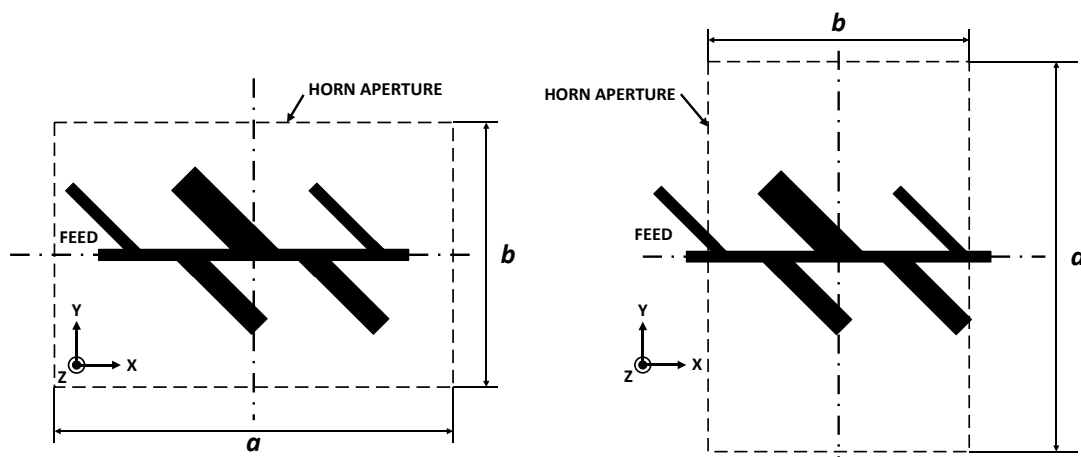


Figure 4.10 Orientations of reference horn antenna with respect to AUT for co-polarization (left) and cross-polarization (right) radiation pattern measurements of 45 degree comb-line array

As discussed earlier, the radiation patterns of both 45 and 90 degree comb-line arrays are oriented in the same way. Thus, the relative arrangement of AUT and reference horn antenna in Figure 4.5 can still be applied to the 45 degree array, as indicated in Figure 4.10.

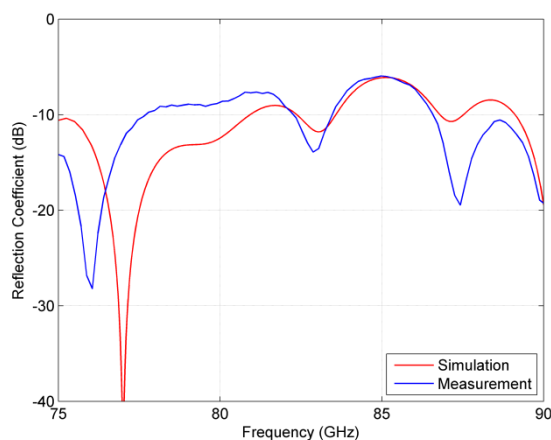


Figure 4.11 Measured and simulated reflection coefficient of the 45 degree amplitude tapered comb-line array

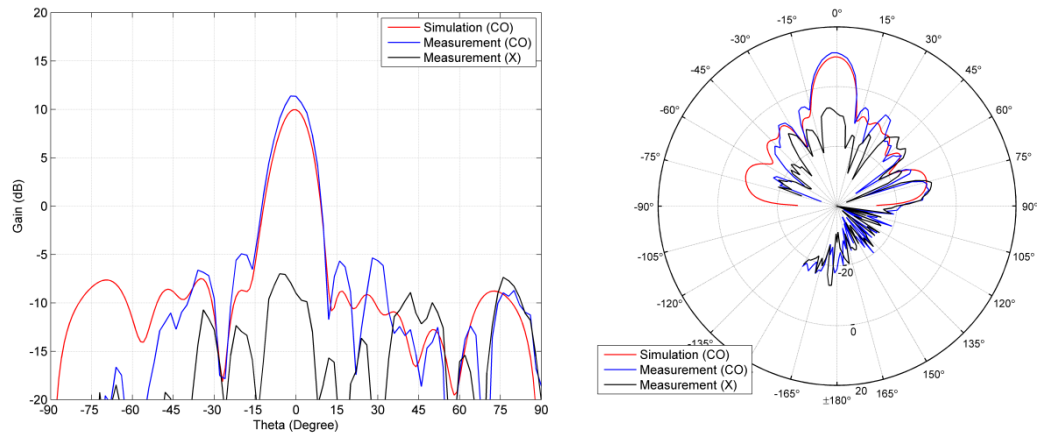


Figure 4.12 Measured and simulated 76.5 GHz xz -plane co-polarization and cross-polarization radiation patterns of the 45 degree amplitude tapered comb-line array plotted in Cartesian coordinate (left) and polar coordinate (right)

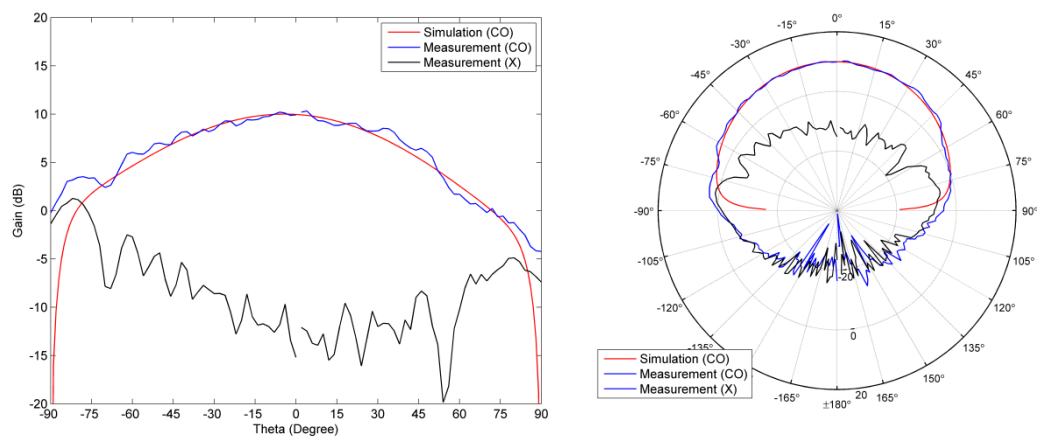


Figure 4.13 Measured and simulated 76.5 GHz yz -plane co-polarization and cross-polarization radiation patterns of the 45 degree amplitude tapered comb-line array plotted in Cartesian coordinate (left) and polar coordinate (right)

The simulation and measurement results of 45 degree amplitude tapered comb-line antenna array are plotted together in Figure 4.11 through 4.13. Around 76.5 GHz the measured reflection coefficient is offset from simulation but still acceptable. In Figure 4.12, the maximum gain of 11.35 dBi is attained at $\theta = -1^\circ$; the HPBW is about 12 degrees and the worst sidelobe level is -16.3 dB. Generally, the measurements agree well with simulations.

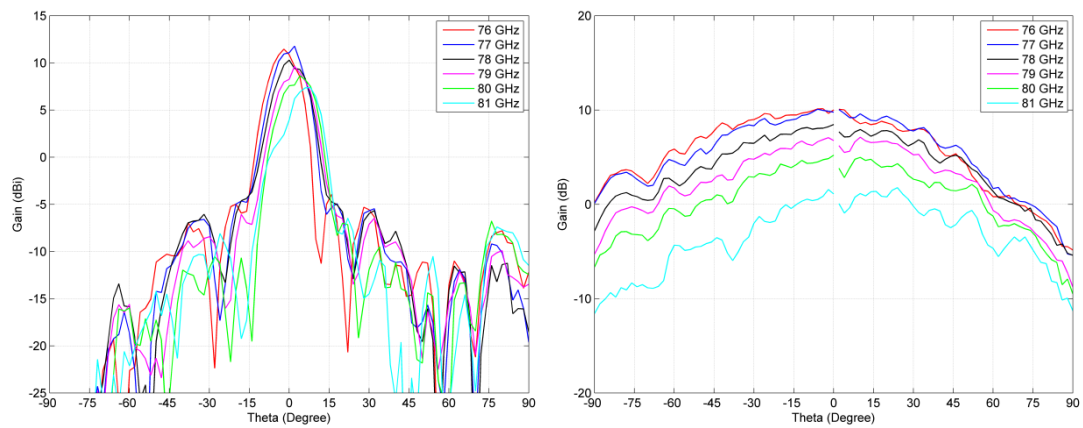


Figure 4.14 Measured xz -plane and yz -plane co-polarization radiation patterns of the 45 degree amplitude tapered comb-line array from 76 to 81 GHz (separated by 1 GHz)

Figure 4.14 shows the co-polarization radiation patterns of 45 degree comb-line array over 76-81- GHz frequency range (separated by 1 GHz). As previous simulation predicts, the performances remain reasonably stable between 76 and 79 GHz but start getting worse from 80 GHz.

5 Conclusion

In this thesis, the design of 76.5 GHz microstrip comb-line antenna array was discussed. In addition to the typical 90 degree array, a 45 degree array was developed especially for automotive radar application. Both arrays were implemented in standing-wave configuration and weighted by 20 dB Taylor amplitude taper. The measurements were performed with a probe-based setup.

The good agreement between simulation and measurement results proves the reliability of ADS Momentum simulator. For the simulations of moderately complex planar structures, Momentum is an appropriate choice since it can deliver fairly accurate results in a relatively short time. Furthermore, by applying probe-based approach, the measurement procedure becomes more accurate, efficient and straightforward.

The subsequent task is to test the fabricated antennas together with the radar prototype module, due to time constraints it is not covered in this thesis. For practical reasons, both aforementioned arrays are fed at the end. Alternatively, the feed point can also be placed at the array center. Future research should investigate the center-fed array and compare its performance with that of the end-fed array.

References

- [1] A. L. Merlo, "Automotive radar for the prevention of collisions," *IEEE Trans. Ind. Electron.*, vol. IECI-11, no. 1, pp. 1-6, Feb. 1964.
- [2] F. R. Holmstrom *et al.*, "A microwave anticipatory crash sensor for activation of automobile passive restraints," *IEEE Trans. Veh. Technol.*, vol. 22, no. 2, pp. 46-54, May 1973.
- [3] J. E. Stevens and L. L. Nagy, "Diplex Doppler radar for automotive obstacle detection," *IEEE Trans. Veh. Technol.*, vol. 23, no. 2, pp. 34-44, May 1974.
- [4] T. Tamama *et al.*, "Radar sensor for automotive collision prevention," in *IEEE MTT-S Int. Microwave Symp. Dig.*, 1978, pp. 168-170.
- [5] J. D. Woll, "Monopulse Doppler radar for vehicle applications," in *Proc. Intelligent Vehicles Symp.*, 1995, pp. 42-47.
- [6] J. Wenger, "Automotive radar – status and perspectives," in *IEEE Compound Semiconductor Integrated Circuit Symp.*, 2005, pp. 21-24.
- [7] H. Daembkes and M. Camiade, "GaAs MMICs for automotive applications," in *28th European Microwave Conf.*, 1998, pp. 630-635.
- [8] S. Trotta *et al.*, "An RCP packaged transceiver chipset for automotive LRR and SRR systems in SiGe BiCMOS technology," *IEEE Trans. Microw. Theory Tech.*, vol. 60, no. 3, pp. 778-794, Mar. 2012.
- [9] Y. Kawano *et al.*, "A 77GHz transceiver in 90 nm CMOS," in *IEEE Int. Solid-State Circuits Conf. Dig. Tech. Papers*, 2009, pp. 310-311.
- [10] Y. Li *et al.*, "A fully integrated 77GHz FMCW radar system in 65nm CMOS," in *IEEE Int. Solid-State Circuits Conf. Dig. Tech. Papers*, 2010, pp. 216-217.
- [11] H. H. Meinel, "Evolving automotive radar – from the very beginnings into the future," in *8th European Conf. Antennas and Propagation*, 2014, pp. 3107-3114.
- [12] H. Rohling, "Milestones in radar and the success story of automotive radar systems," in *11th Int. Radar Symp.*, 2010.
- [13] W. Menzel and A. Moebius, "Antenna concepts for millimeter-wave automotive radar sensors," *Proc. IEEE*, vol. 100, no. 7, pp. 2372-2379, July 2012.

- [14] B. Fleming, "Recent advancement in automotive radar systems," *IEEE Veh. Technol. Mag.*, vol.7, no. 1, pp. 4-9, Mar. 2012.
- [15] J. Hasch *et al.*, "77 GHz radar transceiver with dual integrated antenna elements," in *German Microwave Conf.*, 2010, pp. 280-283.
- [16] A. Fischer *et al.*, "A 77-GHz antenna in package," in *41st European Microwave Conf.*, 2011, pp.1316-1319.
- [17] H. Raza *et al.*, "Resemblance between gap waveguides and hollow waveguides," *IET Microwaves, Antennas & Propagation*, vol. 7, no. 15, pp. 1221-1227, Dec. 2013.
- [18] H. Raza *et al.*, "Microstrip-ridge gap waveguide—study of losses, bends, and transition to WR-15," *IEEE Trans. Microw. Theory Tech.*, vol. 62, no. 9, pp. 1943-1952, Sep. 2014.
- [19] A. A. Brazález *et al.*, "Design of F-band transition from microstrip to ridge gap waveguide including Monte Carlo assembly tolerance analysis," *IEEE Trans. Microw. Theory Tech.*, vol. 64, no. 4, pp. 1245-1254, Apr. 2016.
- [20] A. U. Zaman and P. S. Kildal, "Wide-band slot antenna arrays with single-layer corporate-feed network in ridge gap waveguide technology," *IEEE Trans. Antennas Propag.*, vol. 62, no. 6, pp. 2992-3001, June 2014.
- [21] S. A. Razavi *et al.*, "2×2-slot element for 60-GHz planar array antenna realized on two doubled-sided PCBs using SIW cavity and EBG-type soft surface fed by microstrip-ridge gap waveguide," *IEEE Trans. Antennas Propag.*, vol. 62, no. 9, pp. 4564-4573, Sep. 2014.
- [22] E. Pucci *et al.*, "Planar dual-mode horn array with corporate-feed network in inverted microstrip gap waveguide," *IEEE Trans. Antennas Propag.*, vol. 62, no. 7, pp. 3534-3542, July 2014.
- [23] J. Yin *et al.*, "The circular Eleven antenna: a new decade-bandwidth feed for reflector antennas with high aperture efficiency," *IEEE Trans. Antennas Propag.*, vol. 61, no. 8, pp. 3976-3984, Aug. 2013.
- [24] Y. Yu *et al.*, "A compact UWB indoor and through-wall radar with precise ranging and tracking," *Int. J. Antenna and Propagations*, vol. 2012, Apr. 2012. doi:10.1155/2012/678590
- [25] J. Yang *et al.*, "Impedance matrix of a folded dipole pair under Eleven configuration," *IET Microwaves, Antennas & Propagation*, vol. 4, no. 6, pp. 697-703, June 2010.
- [26] J. Yang *et al.*, "Comparison of two decade-bandwidth feeds for reflector antennas: the Eleven antenna and quadridge horn," in *4th European Conf. Antennas and Propagation*, 2010.

- [27] J. Yang and P. S. Kildal, "FDTD design of a Chinese hat feed for shallow mm-wave reflector antennas," in *IEEE Antennas and Propagation Soc. Int. Symp.*, 1998, pp. 2046-2049.
- [28] J. R. James and G. J. Wilson, "Microstrip antennas and arrays. Pt.1-Fundamental action and limitations," *IEE J. Microwaves, Optics and Acoustics*, vol. 1, no. 5, pp. 165-174, Sep. 1977.
- [29] J. R. James *et al.*, "Gain enhancement of microwave antennas by dielectric-filled radomes," *Proc. IEE*, vol. 122, no. 12, pp. 1353-1358, Dec. 1975.
- [30] R. E. Collin, *Field Theory of Guided Waves*, 2nd ed. New York: Wiley-IEEE Press, 1991, pp.712-715.
- [31] J. R. James and A. Henderson, "High-frequency behaviour of microstrip open-circuit terminations," *IEE J. Microwaves, Optics and Acoustics*, vol. 3, no. 5, pp. 205-218, Sep. 1979.
- [32] Y. Hayashi *et al.*, "Millimeter-wave microstrip comb-line antenna using reflection-canceling slit structure," *IEEE Trans. Antennas Propag.*, vol. 59, no. 2, pp. 398-406, Feb. 2011.
- [33] L. Zhang *et al.*, "Microstrip grid and comb array antennas," *IEEE Trans. Antennas Propag.*, vol. 59, no. 11, pp. 4077-4084, Nov. 2011.
- [34] C. A. Balanis, *Antenna Theory: Analysis and Design*, 3rd ed. New York: Wiley-InterScience, 2005, pp. 406-410.
- [35] R. N. Simons, "Novel on-wafer radiation pattern measurement technique for MEMS actuator based reconfigurable patch antennas," NASA Glenn Res. Cen., Cleveland, OH, Tech. Rep. NASA/TM-2002-211816, Oct. 2002.
- [36] T. Zwick *et al.*, "Probe based MMW antenna measurement setup," in *IEEE Antennas and Propagation Soc. Int. Symp.*, 2004, pp. 747-750.
- [37] S. Ranvier *et al.*, "Compact 3-D on-wafer radiation pattern measurement system for 60 GHz antennas," *Microwave and Optical Technol. Lett.*, vol. 51, no. 2, pp. 319-324, Feb. 2009.
- [38] S. Beer and T. Zwick, "Probe based radiation pattern measurements for highly integrated millimeter-wave antennas," in *4th European Conf. Antennas and Propagation*, 2010.
- [39] H. Gulan *et al.*, "Probe based antenna measurements up to 325 GHz for upcoming millimeter-wave applications," in *Int. Workshop Antenna Technology*, 2013, pp. 228-231.